![HAL open science]

Fossil seamount in southeast Zagros records intraoceanic arc to back-arc transition: New constraints for the evolution of the Neotethys

Guillaume Bonnet, Philippe Agard, Hubert Whitechurch, Marc Fournier, Samuel Angiboust, Benoît Caron, Jafar Omrani

1

2 **Fossil seamount in southeast Zagros records intraoceanic arc to back-arc transition:**

3 **new constraints for the evolution of the Neotethys**

4

5 Bonnet, G.[a,b,*], Agard, P.[a], Whitechurch, H.[c], Fournier, M.[a], Angiboust, S.[e], Caron, B.[a], Omrani,

6 J.[e]

7 [a] Sorbonne Université, CNRS-INSU, Institut des Sciences de la Terre de Paris, ISTeP UMR

8 7193, F-75005 Paris, France

9 [b] now at: Earth Research Institute and Department of Earth Science, University of California,

10 Santa Barbara, CA 93106, USA

11 [c] Institut de Physique du Globe de Strasbourg, EOST-CNRS-UMR 7516, Université de

12 Strasbours, 67000 Strasbourg, France

13 [d] Institut de Physique du Globe de Paris, Sorbonne Paris Cité, Université Paris Diderot, CNRS,

14 F-75005 Paris, France

15 [e] Geological Survey of Iran, Tehran, Iran

16

17 * Corresponding author: gbonnet01@gmail.com

18

19 *Abstract*

20 *The Neotethys ocean is transiently involved in two subduction zones during the Late*

21 *Cretaceous. While the Northern Neotethys subduction zone (below Eurasia) was active from*

22 *the early Mesozoic until the Eocene, the intra-oceanic Southern Neotethys subduction zone*

23 *only developed during the Late Cretaceous. We herein document, through a combination of*

24 *structural, geochemical and geochronological data, the magmatic evolution of a Late*

25 *Cretaceous supra-subduction ophiolite fragment of the Neotethys (the Siah Kuh massif,*

26 *Southern Iran), now sandwiched in the Zagros suture zone. Results show that this ophiolite*

27 *fragment — a subducted yet exceptionally well-preserved seamount — records an evolution*

28 *from supra-subduction zone magmatism (including island arc tholeiites, boninites and calc-*

29 *alkaline transitional magmatism) around 87 Ma, to MORB (from E-MORB to N-MORB)*

30 *magmatism at 78 Ma, and potentially until 73 Ma. We conclude that this seamount initially*

31 *formed in an arc context and represents either (i) a non-obducted remnant of the Oman*

32 *ophiolite that experienced a longer-lived magmatic history (prefered hypothesis) or (ii) a*

33 *piece from the forearc/frontal arc of the Northern margin of the Neotethys. Regardless of its*

34 *exact original location, the Siah Kuh seamount was later subducted in the Northern*

35 *Neotethys subduction zone.*

36

37

38

39

40

41 **1. Introduction**

42 Alike modern ocean floor, ophiolites exposed throughout the world span a range of

43 geochemical signatures, in part reflecting their diverse original tectonic setting: mid-ocean

44 ridges, ocean islands (hotspots), island arcs (Pearce, 2008). On modern ocean floor,

45 seamounts are defined as ''geographically isolated topographic feature[s] on the seafloor

46 taller than 100 m, including ones whose summit regions may temporarily emerge above sea

47 level, but not including features that are located on continental shelves or that are part of

48 other major landmasses'' (Staudigel et al., 2010). While the majority of these seamounts are

49 thought to have formed through hotspot-fed magmatism (and have ocean island basalt –

50 OIB – affinities, e.g. Hawaiian islands), many of them also form along ocean ridges (e.g. at

51 the East Pacific Rise, Batiza and Vanko, 1984; with mid-ocean ridge basalt – MORB –

52 affinities) and in volcanic arc contexts (e.g. Izu-Bonin arc system, Hochstaedter et al., 2001)

53 with island arc tholeiite – IAT – to calk-alkaline affinities).

54 Seamounts are however rarely preserved in the geological record of the ocean floor, i.e.

55 within ophiolitic material. Most of them indeed get subducted (Ranero and von Huene,

56 2000) with only fragments left over (Cloos, 1993), that may even not be recognized as such

57 (unless having an OIB-like signature; e.g. Hauff et al., 1997; John et al., 2010). A few

58 seamounts however escape subduction and are docked in accretionary wedges (e.g. Nicasio

59 Reservoir Terrane, Schnur and Gilbert, 2012) or are shallowly subducted and underplated,

60 but very few are exhumed almost intact. Notable exceptions are the late Paleozoic Anarak

61 and Kabudan seamounts (Bagheri and Stampfli, 2008; Central Iran) and the Mesozoic Snow

62 Mountain (MacPherson, 1983; Franciscan complex, USA), identified according to their

63 structure and OIB signatures.

In the Mesozoic realm of the Neotethys, the geological record is dominated by supra-subduction zone (SSZ) ophiolites, that may represent either forearc ocean floor, oceanic arc or back-arcs (Moghadam and Stern, 2015 and references therein). This preferential record is consistent with the mechanism leading to the obduction of ophiolite, starting from intra-oceanic subduction initiation (Agard et al., 2007; Boudier et al., 1988), forearc spreading (Casey and Dewey, 1984) and leading to continental subduction below the newly formed ophiolite (Searle et al., 2004). Small ocean basins formed in back-arc settings behind continental stripes are also partly preserved during collision (e.g. Agard et al., 2011; Rossetti et al., 2010).

These ophiolitic fragments therefore preserve essential information regarding subduction processes and magmatic evolution on the seafloor. However (with the exception of the extensively studied Semail ophiolite in Oman), most large-scale ophiolites or ophiolitic "mélanges" exposed in the Zagros-Makran orogens are strongly dismembered (Burg, 2018; Whitechurch et al., 2013).

This makes the recently discovered Siah Kuh seamount (Bonnet et al., 2019a) the ideal target to study the continuous evolution and origin of magmatic activity in an ophiolite, with implications for lithosphere formation, mantle heterogeneities and regional geodynamics.

This contribution therefore addresses three major questions:

   (1) In the light of geochemical and geochronological data, what is the origin of the Siah Kuh seamount (i.e., mid-ocean ridge seamount, hotspot/plume related, arc-related)?

   (2) Does the Siah Kuh seamount preserve evidence for progressive changes in magmatism and/or in the nature of the (mantle) source?

   (3) Does this help constrain the former location of the seamount in the Neotethys realm?

To that end, we herein present detailed petrological and geochemical data, i.e. bulk-rock analyses of major, trace elements and Sr-Nd isotopes, as well as dating and Hf isotope analysis of zircons from representative lithologies.

2. Geological setting

2.1. Ocean-floor and arc preservation in the Iran-Oman Neotethys

95   The Zagros-Makran orogen formed through the closure of an allegedly large oceanic basin,

96   the Neotethys ocean (probably larger than 1000 km, Agard et al., 2011; Barrier and

97   Vrielynck, 2008). Remnants of this basin are found in Oman (including the thoroughly

98   studied Semail ophiolite) and in Iran along two ophiolite belts: the Outer and Inner

99   Zagros/Makran ophiolite belts (McCall, 1997; Stöcklin, 1981; Fig. 1a).

100   In the Zagros, the Outer ophiolite belt, located along the Main Zagros Thrust (MZT) includes

101   the (relatively coherent) ophiolitic massifs of Khoy, Kermanshah, Neyriz and Hajiabad-

102   Esfandagheh (from Northwest to Southeast). The Hajiabad (Esfandagheh) ophiolitic

103   exposures (Fig. 1b) are associated with the only blueschist exposures in the Zagros, which

104   led Agard et al. (2006) to interpret the MZT as the Zagros Suture Zone. Dismembered pieces

105   of ophiolites are also found all along the MZT in the so-called "colored mélange" (Gansser,

106   1960).

107   All Zagros ophiolites display a large age spread (except the Neyriz ophiolite, where only Late

108   Cretaceous magmatism was described; Babaie et al., 2006; Lanphere and Pamić, 1983;

109   Monsef et al., 2018a), suggesting different stages of magmatic activity, notably during the

110   Triassic-Liassic and Late Cretaceous to Paleocene periods (Ao et al., 2016; Moghadam et al.,

111   2013b, 2017; Whitechurch et al., 2013). The Triassic-Liassic magmatism usually shows

112   alkaline to MORB signatures, whereas the Late Cretaceous one shows an SSZ signature (Ali et

113   al., 2012; Babaie et al., 2001; Khalatbari-Jafari et al., 2004; Moghadam et al., 2013b, 2014b;

114   Saccani et al., 2013; Whitechurch et al., 2013).

115   The Sanandaj-Sirjan Zone, to the North of the Zagros Suture Zone, is interpreted as a piece of

116   the Eurasian upper plate (e.g. Agard et al., 2011; Ghasemi and Talbot, 2006) that separates

117   the Outer Zagros ophiolite belt from the Inner Zagros ophiolite belt. This belt comprises

118   small dismembered ophiolitic massifs including the Nain, Dehshir, Shahr-e Babak and Baft

119   locations from Northwest to Southeast (abbreviated hereafter as "Nain-Baft"). The

120   magmatism within these units has strong SSZ signatures (Moghadam et al., 2009) and

121   occurred from 'mid' Cretaceous to early Paleocene (Arvin and Robinson, 1994; Moghadam et

122   al., 2013a, 2013c, 2010). Most authors separate the Outer and Inner ophiolite belts, the

123   former being a forearc of a northward-dipping subduction zone (responsible for the Zagros

124   blueschists), the latter being the coeval back-arc (e.g. Agard et al., 2011; Arvin and

125   Robinson, 1994; Moghadam et al., 2009), although some have proposed that both ophiolitic

126   belts belong to the same ophiolite (e.g. Moghadam et al., 2010).

127 McCall (1997) proposed a continuity between the Zagros and the Makran ophiolites. The

128 Outer ("Colored Mélange") and Inner ophiolite belts are separated by the Bajgan-Durkan

129 complex, analogous to the Sanandaj-Sirjan zone. Cretaceous blueschist facies ophiolitic units

130 of the North Makran suture are however located to the north and structurally above all of

131 these units (Hunziker et al., 2017) and suggest a slightly different geological evolution than in

132 the Zagros. In spite of the scarcity of intact ophiolitic exposures in the continuity of the

133 Outer ophiolite belt, the study of dismembered ophiolites allowed the identification of Late

134 Cretaceous (possibly starting during Early Cretaceous) magmatism with dominant SSZ and

135 accessory MORB signatures (Saccani et al., 2018). Ophiolites in the Inner Makran ophiolite

136 belt, including the Band-e Zeyarat/Dar-e Anar, Ganj, Rameshk-Mokhtarabad, Fannuj-

137 Maskutan, Kahiri-Espakeh and Iranshahr ophiolitic massifs testify to an Early Cretaceous

138 magmatic stage, associated with alkaline (OIB) magmatism, and Late Cretaceous SSZ

139 magmatism (Burg, 2018; Ghazi et al., 2004; Kananian et al., 2001; Monsef et al., 2018b).

140 Across the Gulf of Oman, the Semail ophiolite is commonly regarded as having formed

141 during the Late Cretaceous (96-94 Ma; Goodenough et al., 2010; Rioux et al., 2013, 2012;

142 Warren et al., 2005), in a SSZ context with increasing maturity, yet never reaching a mature

143 arc stage (Alabaster et al., 1982; Godard et al., 2003).

144 Given the variety of Late Cretaceous ophiolitic remnants from the Neotethys, linking them to

145 a specific geodynamic context may prove difficult (see the schematic paleogeographical map

146 on Fig. 1c). Exceptional pieces of oceanic lithosphere like the Siah Kuh seamount may help

147 constraining the paleogeography of the Iran-Oman transect, with critical inference for

148 regional-scale geodynamics.

149

150   2.2.   The Siah Kuh massif, an exhumed seamount

151 The Siah Kuh unit is a 18x12 kilometer-wide and >1.5 km-high coherent portion of ocean

152 floor (Fig. 2a,b) belonging to the Hajiabad ophiolite, close to the transition between Zagros

153 and Makran. At variance to earlier map reports ("colored mélange", Azizan et al., 2007;

154 Madjidi et al., 1993; Nazemzadeh et al., 2007), this unit is a coherent magmatic unit with

155 some sediments and subordinate serpentinite only. It is tectonically overlain by blueschist

156 facies units metamorphosed during Late Cretaceous (Agard et al., 2006; Angiboust et al.,

157 2016; Moghadam et al., 2017; Monié and Agard, 2009; Sabzehei, 1974) and by rocks of the

158 Sanandaj-Sirjan zone (locally represented by the Sikhoran ultramafic-mafic complex (itself

159   capped by metasediments of the Sargaz-Abshur unit, Ahmadipour et al., 2003; Ghasemi et

160   al., 2002). The so-called Siah Kuh granitoids (Arvin et al., 2007) dated to 200 Ma, are located

161   to the North and thrust upon the Siah Kuh unit of this paper, but are not part of it.

162   The architecture of the Siah Kuh unit is summed up on Fig. 2 (after Bonnet et al., 2019). The

163   Siah Kuh unit is separated into two sub-units (A and B) by a major, km-scale thrust. The A

164   unit is characterized by a magmatic core (A_1) stratigraphically overlain by reef limestone and

165   pelagic sediments, upon which new lavas are erupted (Fig. 2c and Fig. 3a,b).

166   The core of the A unit (A_1) is made of pillow basalts (Fig. 3c) and breccias, intruded by felsic

167   magmatic rocks (Fig. 3d). Moghadam et al. (2013b) reported boninite lavas in this part of the

168   Siah Kuh unit (although the location of these samples is approximate – near the Avenân

169   village, see Fig. 2a – they are unambiguously within and close to the top of the A_1 unit). The

170   felsic intrusions are associated with rhyo-dacitic lava flows on top of the basalts.

171   The lava flows of the core A_1 unit are stratigraphically overlain by up to 400 meters of

172   deepening-up oceanic sediments (Fig. 3a,b,d). The basal sediment is reef to lagoon-like with

173   remains of foraminifera, urchin spines and gastropods (Bonnet et al., 2019a), but is locally

174   absent. Deeper sediments constituted of tuffaceous sandstone, clays, radiolarite and pelagic

175   limestone are deposited above this shallow limestone, all of which are locally infiltrated by

176   felsic sub-volcanic material. These sediments are assumed to be of Campanian to

177   Maastrichtian age in former studies (84-66 Ma; Sabzehei, 1974).

178   Up to 1 km-thick pillow basalts and basaltic flows (units $A_{1'}$-A_2-A_3-A_4 of Fig. 2a) have been

179   erupted directly on top of the sediments (Fig. 3a,b). While the contact between the A_1 unit

180   and $A_{1'}$-A_2-A_3-A_4 was very often reworked by faults parallel to the sedimentary layer, the

181   original unfaulted, stratigraphic contact is preserved in some places (such as between A_1 and

182   $A_{1'}$, Fig. 2a). This large volume of lavas, marking the resumption of volcanic activity after

183   some period of magmatic inactivity, is described as a "rejuvenation event" in Bonnet et al.

184   (2019). We later separate this rejuvenation event in "early-stage rejuvenation" for the lavas

185   located just above the sediments and "late-stage" for lavas higher in the sequence. As

186   pointed out by Bonnet et al. (2019), the A unit as a whole has all the characteristics of a

187   seamount (i.e. a bathymetric anomaly on the seafloor).

188   The second sub-unit (Unit B) has a serpentinized ultramafic base intruded by an anorthosite

189   dike (Fig. 3e) and rodingite pods. A large volume of gabbro overlies the ultramafics, with

190   fining-upwards grain size. A 300 m-thick body of felsic volcanics overlain by a thin and very

191   discontinuous layer of pelagic sediments is intercalated in coarse-grained gabbros and
192   diabase (Fig. 3f). In the southern part of the B unit, gabbros are overlain by basalts. The
193   abundance of felsic rocks (rare in ophiolitic rocks from adjacent areas) and sedimentary
194   intercalations that can be correlated with the structure of the A unit suggest that this unit
195   could be a lateral equivalent of the seamount core.

196   The whole Siah Kuh seamount was then subducted to ~30 km depth, as attested by very
197   incipient high-pressure metamorphism marked by lawsonite and aragonite crystallization
198   (e.g. Fig. 4d,e). It was subsequently exhumed as an intact piece, with limited subduction-
199   related deformation (these aspects, beyond the scope of the present study, are detailed in
200   Bonnet et al., 2019a, 2019b).

201

202   **3. Sampling and analytical methods**

203   Approximately 100 samples of magmatic rocks and serpentinized ultramafics were collected
204   in different units of Siah Kuh, including the core of the seamount, the early and late stages of
205   the magmatic rejuvenation, gabbros, diabase and basalt of the B unit, as well as felsic
206   volcanics and subvolcanics. After examination of thin sections, 36 samples were selected for
207   detailed analyses (Table 1). The precise GPS location of each sample is given in
208   Supplementary Material S1.

209   An aliquot of each magmatic sample (31 samples) was crushed and powdered for 30 minutes
210   with an electric mortar in agate to avoid contamination. These samples were finely crushed
211   to <2 μm grains for major, trace and Sr-Nd isotopes analyses. About 4 g of each sample was
212   dried at 110°C in an alumina crucible and heated twice for one hour to 1000°C and
213   reweighted for loss on ignition calculation.

214   Major elements analyses were performed at ALIPP6 (Sorbonne Université) by ICP-OES
215   spectroscopy (with an Agilent 5100 SVDV ICP-OES) after dissolution at 80°C with HNO_3 and
216   HF and neutralization with $B(OH)_3$. Trace element analyses were also performed at ALIPP6
217   (Sorbonne Université) through QQQ-ICP-MS spectroscopy (using an Agilent 8800 ICP-QQQ-
218   MS) after dissolution at 80°C with HNO_3 and HF and neutralization with HNO_3 and H_3BO_3.

219   Detailed analyses are provided in Supplementary Material S2. Geochemical data were
220   normalized to the primitive mantle values and chondrite values (Sun and McDonough,
221   1989).

222   12 samples were selected for bulk rock Sr-Nd isotopic analyses (performed at SARM, Nancy).

223   εNd_i and $^{87}Sr/^{86}Sr(t)$ values were calculated on the basis of their expected ages

224   (Supplementary Material S3). These corrections change the εNd and $^{87}Sr/^{86}Sr$ values by a

225   maximum of 0.7 and 0.00001, respectively.

226   Clinopyroxene and spinel compositions of 10 basaltic samples and 5 serpentinites have been

227   analyzed using a Cameca SX100 electron microprobe (15 kV, 10 nA, 1 µm spot, WDS) at

228   CAMPARIS (Sorbonne Université), with diopside (Si, Ca, Mg), orthoclase (K, Al), $MnTiO_3$ (Mn,

229   Ti), Fe_2O_3 (Fe) and albite (Na) as standards. The analyses were sorted and Fe^{3+}

230   concentrations were estimated using the method exposed by Droop (1987). Analyses are

231   provided in Supplementary Materials S4 and S5.

232   Four samples were coarsely crushed and zircon grains were separated for U-Pb dating and Hf

233   isotope analysis, using conventional heavy fraction and magnetic techniques. Zircon grains

234   were placed on epoxy mounts and then polished to expose their half-sections, which were

235   photographed under transmitted and reflected light using an optical microscope to reveal

236   internal cracks and mineral inclusions. Cathodoluminescence (CL) images of the zircon grains

237   were generated using a LEO1450VP scanning electron microscope (SEM) with an attached

238   Gatan MinCL detactor at IGGCAS (Supplementary Material S6).

239   U-Pb dating and trace element analysis of zircons from 4 samples were simultaneously

240   conducted by LA-ICP-MS at the Wuhan SampleSolution Analytical Technology Co., Ltd.,

241   Wuhan, China. Detailed operating conditions for the laser ablation system and the ICP-MS

242   instrument and data reduction are the same as description by Zong et al. (2017). Laser

243   sampling was performed using a GeolasPro laser ablation system that consists of a

244   COMPexPro 102 ArF excimer laser (wavelength of 193 nm and maximum energy of 200 mJ)

245   and a MicroLas optical system, with a spot size of 32 µm. An Agilent 7700e ICP-MS

246   instrument was used to acquire ion-signal intensities. Helium was applied as a carrier gas.

247   Argon was used as the make-up gas and mixed with the carrier gas via a T-connector before

248   entering the ICP. A "wire" signal smoothing device is included in this laser ablation system

249   (Hu et al., 2015). Zircon 91500 and glass NIST610 were used as external standards for U-Pb

250   dating and trace element calibration, respectively. Each analysis incorporated a background

251   acquisition of approximately 20-30 s followed by 50 s of data acquisition from the sample.

252   An Excel-based software ICPMSDataCal was used to perform off-line selection and

253   integration of background and analyzed signals, time-drift correction and quantitative

254 calibration for trace element analysis and U-Pb dating (Liu et al., 2010, 2008). Common-Pb

255 correction was done using the method of Andersen (2002). Data reduction was carried out

256 using the Isoplot/Ex v. 2.49 programs (Ludwig, 2001). Analyses of reference zircon Plešovice

257 as an unknown give an accurate date within uncertainty (338.4 ± 1.9 Ma, compared to

258 337.13 ± 0.37; Sláma et al., 2008). U-Pb and trace element analyses of zircons are provided

259 in Supplementary Material S7, S8 and S9.

260 In-situ zircon Lu-Hf isotopic analyses were carried out using a Neptune MC-ICP-MS with an

261 ArF excimer laser ablation system. Hf isotopic analyses were obtained on the same zircon

262 grains that were previously analyzed for LA-ICP-MS U-Pb isotopes, with ablation pits of 32-65

263 μm in diameter and a laser repetition rate of 10 Hz with 100 mJ was used. Details of the

264 technique are described by Wu et al. (2006). Decay constant by Söderlund et al. (2004) and

265 present-day chondritic ratios by Bouvier et al. (2008) were adopted to calculate εHf(t)

266 values. The single stage model age (T_{DM}) was calculated by using the present-day depleted

267 mantle isotopic ratios (Supplementary Material S10, Vervoort and Blichert-Toft, 1999).

268

269 ## 4. Petrography

270 A summary of the mineralogical assemblages is provided in Table 1. We report on Fig. 4

271 pictures of representative textures from mafic rocks in A (Fig. 4a-c), in B (Fig. 4d-f) and felsic

272 rocks in A (Fig. 4g) and B (Fig. 4h,i).

273

274 **Mafic lavas**

275 Mafic lavas are the main constituent of unit A and of the top of B (Fig. 2). They are all

276 basaltic, with clinopyroxene, plagioclase and Fe-Ti oxides in a glassy matrix (Fig. 4a-c,f). Most

277 samples show evidence of hydrothermal alteration, marked by the growth of secondary

278 phases. Pumpellyite, epidote and chlorite usually replace primary clinopyroxene and volcanic

279 glass, while primary plagioclase is often albitized. Quartz, calcite, epidote, prehnite, and

280 pumpellyite fill vesicles and veins that result from strong degassing of magmas during

281 eruption (eg. Fig. 4f). Green amphibole is found in one basalt. Clinopyroxene phenocrysts are

282 more frequent in the A_1 unit, but generally units cannot be distinguished solely based on

283 magmatic textures.

284 A few samples show crystallization of high-pressure minerals during subduction, such as
285 lawsonite and pumpellyite replacing plagioclase in one sample, or more frequently
286 aragonite-bearing veins (see Bonnet et al., 2019 for more details).

287

288 **Gabbros and diabase**

289 Gabbroic rocks are found within the B unit. They are mainly made of plagioclase surrounded
290 by clinopyroxene, with oxide and rare olivine. One sample (#1532) was recovered in a
291 sequence with strong grain size variations (potentially cumulitic). Poikilitic textures are
292 observed in the zones of smaller grain size (Fig. 4d). Hydrothermal minerals include
293 amphibole and chlorite replacing clinopyroxene and serpentine replacing rare olivine. High-
294 pressure metamorphism is common in these samples with lawsonite and pumpellyite
295 replacing plagioclase (Fig. 4d,e).

296

297 **Felsic lavas**

298 Felsic lavas in A are mainly rhyolites, with large hexagonal quartz crystals, crystals of
299 orthoclase and oxides in a glassy matrix (Fig. 4g). K-feldspar and glass are usually altered to
300 pumpellyite, epidote and chlorite. One rhyolite also contains aragonite and lawsonite in
301 veins.
302 Felsic lavas in B are dacitic, with abundant plagioclase, quartz and oxides in a glassy matrix
303 (Fig. 4e). Plagioclase is albitized and the glass is altered to epidote and chlorite during
304 hydrothermalism.

305

306 **Felsic intrusives**

307 Felsic intrusives are observed within the A units. They are composed of quartz, plagioclase
308 and K-feldspar. They are characterized by the crystallization of secondary epidote, possibly
309 replacing unidentified primary phases.

310

311 **Anorthosite**

312 One anorthosite dyke (#1720) was found in serpentinized ultramafics at the base of the B
313 unit. It is composed of 95% plagioclase, 4% titanite and contains some zircons (Fig. 4i).

314

315 **Ultramafic material**

316 Ultramafics are found within both the A and B units, and are close to 100% serpentinized
317 (chrysotile-lizardite, except for spinel that is generally preserved). One sample of
318 serpentinized ultramafics from the A unit is likely a former dunite with two generations of
319 Al-Cr-rich spinel distinguished by their color.

320 By contrast, ultramafics of the B unit more likely represents a former harzburgite or a
321 cumulate ultramafic sequence, with little-deformed patches of former olivines, and
322 abundant bastite replacing former pyroxene, whose cleavage is revealed by Fe-Ti oxides. A
323 chromitite pod within the ultramafics of the B unit is made of 90% of Cr-spinel and 10%
324 serpentine.

325 Spinel is the main aluminium-bearing phase in all ultramafic samples. All samples also have
326 secondary magnetite crystallization around serpentinized olivine domains.

327

328   **5. Bulk rock geochemistry**

329 The whole Siah Kuh volcanic sequence has been affected by hydrothermal alteration, as
330 shown by the widespread occurrence of secondary phases such as chlorite and pumpellyite
331 (e.g. Fig. 4f). This is further evidenced by addition of H_2O, as attested by the 0.9 to 8.5 wt.%
332 loss on ignition of the rocks (the loss on ignition may in part correspond to CO_2 loss, from
333 minor secondary carbonate vesicles). To avoid any bias due to major element mobilization
334 during hydrothermal alteration and/or high-pressure metamorphism, we only present
335 diagrams based on elements assumed to be immobile (see discussion in paragraph 9.1).
336 Immobile-element-based classifications of mafic rocks are shown on Fig. 5, trace element
337 spectra on Fig. 6 and trace-element based discrimination diagrams on Fig. 7.

338

339 **Core of the seamount (A$_1$)**

340 Mafic rocks from the core of the seamount plot in the subalkaline basaltic field in the Zr/Ti –
341 Nb/Y diagram (Pearce, 1996; Fig. 5a) and in the tholeiitic basalt to andesite fields in the Th –
342 Co diagram (Hastie et al., 2007; Fig. 5b). REE diagrams (Fig. 6a) show low LREE content
343 compared to MREE and HREE (with very low REE contents for two samples: <5*chondrite for
344 LREE and <8*chondrite for HREE). These rocks have trace element signatures very similar to
345 the lower V2 lavas from Oman (Alabaster et al., 1982; Godard et al., 2003; Kusano et al.,
346 2014). Multielementary spider diagrams (Fig. 6b) show strong Nb-Ta negative anomalies,
347 and small Ti negative anomalies. They plot in the IAT field on the Th/Yb – Nb/Yb (Pearce,

348   2008a; Fig. 7a), in the arc field of the V – Ti diagram (Shervais, 1982; Fig. 7b) and in the IAT

349   and calc-alkaline fields of the Th – Hf – Ta diagram (Wood, 1980; Fig. 7c). They range

350   between MORB and arc basalts in the Th/La – Sm/La diagram (Plank, 2005; Fig. 7d). One

351   sample (#1628) shows Th and LREE enrichment and plots in or close to the calc-alkaline field

352   of the former diagrams.

353

354   **Boninites**

355   Boninites from the core of Siah Kuh were not analyzed in this study, but we herein report

356   bulk-rock analyses by Moghadam et al. (2013b). They are classified as subalkaline basalts in

357   figure 5a, and as tholeiitic basalts to andesites in figure 5b. REE diagrams show strong

358   depletion in LREE compared to HREE (Fig. 6a). They are chemically very close to Oman

359   boninites (upper V2, Ishikawa et al., 2005, 2002; Kusano et al., 2014). They plot in the IAT

360   field in figure 7a and in the boninite field in figure 7b.

361

362   **Felsic rocks**

363   Felsic rocks plot in the subalkaline basaltic andesite/andesite field in figure 5a, except for

364   one sample in the dacite/rhyolite field (despite being petrographically dacites and rhyolites

365   or subvolcanic equivalents) and in the tholeiitic dacite/rhyolite field in figure 5b. No obvious

366   difference exists between the felsic rocks of the A_1 unit and those of the B unit (apart from a

367   smaller Ti negative anomaly in the latter). They have flat to slightly decreasing REE patterns,

368   with marked negative Eu anomaly (Fig. 6c). Multi-elementary spider diagrams show strong

369   Nb-Ta and Ti negative anomalies, and small Zr negative anomalies (Fig. 6d). They also plot in

370   the IAT fields in figures 7a and 7c (except for one sample plotting in the calc-alkaline field;

371   the use of those diagrams is however contested for felsic rocks; Pearce, 2008a). They mainly

372   plot as arc lavas in the Th/La – Sm/La diagrams, with higher Th/La ratios than other rocks.

373

374   **Early stage rejuvenation (A unit: $A_{1'}$ and A_2)**

375   Lavas from the early rejuvenation stage plot as subalkaline in figure 5a, and as tholeiitic

376   basalts in figure 5b. They are enriched in LREE compared to HREE (Fig. 6e). Multi-elementary

377   spider diagrams show no significant HFSE negative anomaly (Fig. 6f). They plot in-between E-

378   MORB and N-MORB in figure 7a, and in the MORB – back-arc basalt field in figure 7b. They

379   are in the E-to-N-MORB transition zone of figure 7c, and are classified as MORB in figure 7d.

380

Late stage rejuvenation (A unit: $A_{1'}$ and A_4)

Rocks from the late stage rejuvenated magmatism are classified as subalkaline basalts in figure 5a and as tholeiitic basalts to andesites in figure 5b. They have bell-shaped REE patterns with depletion in LREE and slight depletion in HREE compared to MREE (Fig. 6e). Multi-elementary spider diagrams show very small Nb-Ta and Ti negative anomalies (Fig. 6f). They plot close to N-MORB in figure 7a and in the MORB – back-arc basalt field of figure 7b. They are classified as N-MORB in figure 7c, and as MORB (yet closer to the OIB field the the early-stage rejuvenation lavas) in figure 7d.

B unit diabases

Samples from the base of the B unit are classified as subalkaline in figure 5a and as tholeiitic basalts in figure 5b. They are enriched in LREE, but have almost flat MREE-HREE trend (Fig. 6g). Multi-elementary spider diagrams show small positive Nb-Ta anomalies but strong negative Zr-Hf anomalies (Fig. 6h). They plot very close to E-MORB in figure 7a and in the MORB-BABB field of figure 7b. They plot in the E-MORB to OIB basalt transition in figure 67c and 7d.

B unit basalts

Basalts from the top of the B unit are classified as subalkaline basalts in figure 5a and as tholeiitic basalts in figure 5b. They have again a flat, slightly bell-shaped REE patterns with a small enrichment in MREE compared to LREE and HREE (Fig. 6g). Multi-elementary spider diagrams show an insignificant negative Ti anomaly (Fig. 6h). They plot in-between the N- and-E-MORB fields of figures 7a and 7c, in the MORB-BABB field of figure 7b, and in the MORB field of figure 7d..

Anorthosite

Its REE pattern has high LREE to HREE ratio and a strong positive Eu anomaly, characteristic of plagioclase (Fig. 6c). Multi-elementary spider diagrams show Zr-Hf and Ti negative anomalies (Fig. 6d).

Gabbros of the B unit

412 Two gabbros within the B unit show very distinct geochemical signatures (Fig. 6g,h). One

413 (#1738) has a REE profile very similar to the diabase of the B unit, with similar positive Nb-Ta

414 positive anomalies and Zr-Hf negative anomalies but with a positive Ti anomaly. The other

415 one (#1532, dated) has enriched MREE and HREE compared to LREE, with a positive Eu

416 anomaly and small negative Ti anomaly. The later resembles the N-MORB-like basalts from

417 the top of the B unit, but is more depleted, probably due to cumulative effects.

418

419 **6. Radiogenic (Sr and Nd) isotope analyses**

420 Representative samples from all extrusive sequences presented above have been analyzed

421 for Sr-Nd isotopes. Results are presented on Fig. 8.

422 All samples are relatively clustered in εNd_i with positive values between 6.68 and 9.21.

423 $^{87}Sr/^{86}Sr(t)$ is relatively more dispersed with values between 0.7045 and 0.7063. All rocks

424 plot out of the mantle correlation line (Fig. 8). There is a progression from high $^{87}Sr/^{86}Sr(t)$

425 values (around 0.7063) for the core of the seamount to lower values in the felsic rocks

426 (around 0.7055-0.706), and even lower values for the rejuvenation event in A and in the

427 mafic rocks of the B unit (between 0.7045 and 0.7055). Isotopic data on the Siah Kuh lavas

428 are comparable with data from other regional ophiolites (Fig.8; Oman: Godard et al., 2006;

429 Neyriz: Moghadam et al., 2014; Nain-Baft: Moghadam et al., 2013c).

430

431 **7. Mineral chemistry**

432 Bulk-rock analyses might be affected by hydrothermal alteration on the seafloor.

433 Consequently, compositions of unaltered clinopyroxenes and spinels in the rocks were

434 measured as they may yield direct information on the magmatic source. Compositional plots

435 for clinopyroxene are shown on Fig. 9a,b,c (after Leterrier et al., 1982) and for spinel on Fig.

436 9d (after Dick and Bullen, 1984). Detailed analyses of clinopyroxene and spinel are available

437 in the Supplementary Materials S1 and S2.

438

439 **Core of the seamount (A$_1$)**

440 Clinopyroxenes have low Ca+Na between 0.75-0.9 atoms per formula unit (apfu), low Ti

441 content (< 0.015 apfu) which place them in the tholeiitic to calc-alkaline basalt field of figure

442 9a, usually low Ti+Cr (average at 0.01 apfu) and high Ca (0.7-0.9 apfu) placing them in the

443   orogenic basalt field of figure 9b. Due to their low Ti content, they plot in the island arc

444   tholeiite field of figure 9c.

445

446   **Early rejuvenation in A**

447   Clinopyroxenes have higher Ti concentration of 0.02-0.04 apfu and low Ca+Na around 0.5-

448   0.8 apfu, high Ti+Cr (0.02-0.035 apfu), which place them in the mid-ocean ridge tholeiite

449   field of figures 9a and 9b.

450

451   **Late rejuvenation in A**

452   Clinopyroxenes have low Ca+Na concentration of 0.7-0.9 apfu, placing them in the

453   subalkaline field, and high Ti+Cr of 0.02-0.05 apfu placing them in the mid-ocean ridge

454   tholeiite field of figures 9a and 9b.

455

456   **B unit gabbro**

457   Clinopyroxenes from sample 1532 have Ca+Na concentrations between 0.85 and 0.92 apfu,

458   placing them mostly in the subalkaline field (Fig. 9a), and high Ti+Cr of 0.03-0.035 apfu

459   placing them in the mid-ocean ridge tholeiite field in figure 9b.

460

461   **B unit diabase**

462   Clinopyroxenes have low Ca+Na concentration between 0.7-0.8 apfu, placing them in the

463   subalkaline field (Fig. 9a), and high Ti+Cr of 0.02-0.045 apfu placing them in the mid-ocean

464   ridge tholeiite field in figure 9b.

465

466   **B unit basalt**

467   Clinopyroxene has 0.75-0.85 apfu Ca+Na, placing them in the subalkaline field (Fig. 9a), and

468   high Ti+Cr of 0.02-0.04 apfu placing them in the mid-ocean ridge tholeiite field (Fig. 9b).

469

470   **Spinel in ultramafic rocks**

471   Two generations of spinels have been analyzed in an ultramafic rock from A, with similar

472   lobate (magmatic) textures yet no textural relationships (Fig. 9d, Supplementary Material

473   S5). One has Cr# of 0.44-0.54, Mg# of 0.60-0.66 and Ti < 0.0018 apfu, while the other has

474   higher Cr# of 0.69-0.75, Mg# of 0.50-0.55 and Ti of 0.0010-0.0032 apfu. The first generation

475 plots in the overlap between the abyssal and supra-subduction fields, while the second

476 generation has clear supra-subduction signatures (Fig. 9d). Spinels in ultramafics from B have

477 a wide range of Ti concentrations (0.002-0.025 apfu), a likely indicator of a cumulative origin.

478 The Ti content increases toward the top of the ultramafic sequence. The lowermost spinels

479 compare with the first generation of the A unit, with similar Cr# (0.46-0.52) but slightly lower

480 Mg# (0.66-0.7).

481

482 **8. Zircon U-Pb dating and Hf isotope analyses**

483 Zircons have been separated from four different kinds of rocks, belonging to the A unit

484 (#1518, rhyolite) and the B unit (#1720, anorthosite; 1532, gabbro; 1432, basalt). Zircons are

485 abundant in anorthosite and gabbro, but scarce in rhyolite and basalt. Most of them have

486 clear magmatic textures (Supplementary Material S3). Only concordant zircons were

487 considered. Zircon cathodoluminescence images, trace element analyses and trace element

488 diagrams are available in the Supplementary Materials S3, S4 and S5 respectively.

489

490 **Rhyolite in A**

491 Despite the small number of zircons in the rock, five concordant zircons show strong

492 inheritance with ages scattered between 1800 and 87 Ma (Fig. 10a). The youngest zircon

493 population (n=2) defines a maximum age with a weighted average of 87.0 ± 1.8 Ma. These

494 two zircons have positive εHf around 10, and T_{DM} ages around 500 Ma (Fig. 11).

495

496 **Gabbro in B**

497 Thirteen concordant zircons yield a weighted average age of 77.8 ± 0.98 Ma (Fig. 10b). Single

498 $^{238}U-^{206}Pb$ ages are scattered between 81 and 75 Ma. All the zircons have very positive εHf

499 values around 14 and T_{DM} ages around 270 Ma (Fig. 11).

500

501 **Anorthosite in B**

502 Fourteen concordant zircons yield a weighted average age of 77.3 ± 1.5 Ma (Fig. 10c). Single

503 $^{238}U-^{206}Pb$ ages are scattered between and 82 and 73 Ma. Most of these zircons have

504 positive εHf values around 9 and T_{DM} ages around 540 Ma (Fig. 11).

505

506 **B unit basalt**

507 Despite the small number of zircons in the rock, five concordant zircons show strong

508 inheritance with ages scattered between 500 and 73 Ma (Fig. 10d). The youngest zircon

509 population (n=2) defines a maximum age for this basalt with a weighted average of 73.7 ±

510 1.3 Ma, with very distinct εHf values of -3 and 16 (Fig. 11).

511

512 **9. Discussion**

513 ***9.1. Effects of seafloor alteration and metamorphism***

514 Seafloor alteration and metamorphism can modify significantly the chemical composition of

515 ophiolitic rocks. Major elements can vary a lot through intense hydration of rocks

516 (represented by LOI, from 0.9 to 8.6 wt.%). Here, most of the hydration occurs at the

517 seafloor, as attested by the appearance of chlorite, epidote and pumpellyite (e.g. Fig 4d,f).

518 Examining correlations between the amount of volatiles in the rock (LOI) and major and

519 trace-elements concentrations (Humphris and Thompson, 1978) can help decipher alteration

520 effects in the rock. In the studied samples Si and Na are inversely correlated with the LOI,

521 even when not considering felsic rocks that are usually much less hydrated than basalts

522 (Supplementary Materials S6). Bulk rock major elements such as Si, Na, K, Ca and trace

523 elements including Cs, Rb, Ba, Sr (LILE) are modified by seafloor alteration (Frey and Weis,

524 1995; Gillis, 1995), questioning the relevance of the TAS and AFM diagrams for altered

525 oceanic rocks. Relict clinopyroxenes are likely trustworthy indicators of the chemistry of the

526 magma, as they are primary minerals with a composition that is governed at first order by

527 the partition coefficients of elements with the magma (Leterrier et al., 1982). Destabilization

528 or recrystallization of clinopyroxene is harder than that of plagioclase (e.g. Spilde et al.,

529 1993).

530 Instead, most high field strength elements (HFSEs), and rare earth elements (REEs) are

531 generally considered to be immobile during alteration (e.g. Cann, 1970). Rock classification

532 based on immobile elements should however be used with care, and cannot replace a

533 careful petrographic examination, as rhyolites in our study were misclassified as andesites in

534 the Zr/Ti – Nb/Y. Trace element ratios used in discrimination diagrams as well Sr, $^{87}Sr/^{86}Sr(t)$,

535 Nd and εNd$_i$ values show no correlation with LOI (Suppl. Material S11). Seawater alteration is

536 however commonly cited as one of the main factors affecting $^{87}Sr/^{86}Sr$ signatures of altered

537 lavas (Hauff et al., 2003; Kawahata et al., 2001). A careful examination of the Sr isotopic

538 signatures shows a negative correlation between the Sr or REE and $^{87}Sr/^{86}Sr$ (Suppl. Material

539   S12), trending toward seawater compositions This is best explained by a relatively stronger

540   effect of seawater alteration on rocks that initially contain little Sr, i.e. the most depleted

541   rocks.

542   Incipient blueschist metamorphism of the whole Siah Kuh unit (at ~200-250°C, 0.6-0.9 GPa)

543   should also be considered as it is associated with fluid circulation (Bonnet et al., 2019a).

544   However, rocks never fully equilibrate at these conditions making the metamorphic imprint

545   very limited (and restricted to some magmatic rocks of the B unit). Associated fluid

546   circulations at T<300°C make alteration during metamorphism less likely than alteration at

547   the seafloor. Further we only discuss the petrogenesis based on alleged immobile elements.

548

549   ### *9.2.   Evolution of geochemical signatures and tectonomagmatic setting*

550   The Siah Kuh seamount is the ideal place to study the evolution of the magmatic source of

551   an ophiolite: unlike most ophiolitic "mélanges" or large-scale ophiolites (save the Oman

552   ophiolite), the structural framework as well as relative and absolute magmatic chronologies

553   are well-constrained here. Furthermore, the Siah Kuh seamount records the evolution of

554   lava chemistry in a single area, so that variations through time may reflect either mantle

555   heterogeneities, viscous flow and/or chemical changes of the composition through time (i.e.,

556   due to melt extraction, fluid circulation or source mixing).

557

558   **An initial supra-subduction event**

559   The supra-subduction origin of altered magmatic rocks may be reflected by four mostly

560   independent trends in the trace elements: (1) rare-earth elements-depleted melts (due to

561   the melting of an already depleted mantle, König et al., 2010), (2) HFSE (including Ti, Nb, Ta,

562   Zr, Hf) depletion compared to REE elements (due to trapping by refractory phases such as

563   Fe-Ti oxides; Briqueu et al., 1984; Gao et al., 2007), (3) V enrichment due to oxidizing

564   conditions above subduction zones enhancing the solubility of V (Shervais, 1982), and (4)

565   enrichment of the source in LREE and Th by sediment-derived fluids (including melts, König

566   et al., 2010; Plank, 2005). The contamination of the source by sediment-derived melts also

567   leads to a strong decrease of εNd toward sedimentary values (around -8, Plank and

568   Langmuir, 1998; e.g. Kusano et al., 2017). These trends are variably observed in the rocks

569   from the A_1 unit (core of the seamount) and in the felsic rocks of B.

570   The lowermost basalts in A_1 are slightly depleted in rare-earth elements (Fig. 6a), in HFSE

571   (Nb-Ta and small Ti negative anomalies, Fig. 6b and Fig 7a,b,c), but do not show enrichment

572   in Th or V (except for one sample, #1628, that is higher in the sequence; Fig. 7a,d). These

573   signatures are typical of arc tholeiites. Clinopyroxene compositions from the A_1 basalts also

574   show sub-alkaline signatures and are comparable to IAT clinopyroxenes (Fig. 9). Sr-Nd

575   isotopes have clustered values of εNd (6.93-7.57), yet variable Sr isotopic ratios (0.70551-

576   0.70633; Fig. 8). The high εNd values preclude any significant contribution from sediments

577   melts to the mantle source. High $^{87}Sr/^{86}Sr$ values are best explained by hydrothermal

578   alteration of the basalts (Suppl. Material S12), as is commonly expected for altered oceanic

579   rocks (e.g. Godard et al., 2006; Hauff et al., 2003; Kawahata et al., 2001).

580   Felsic rocks from A and B have uniform chemical compositions, with a strong depletion in

581   HFSE (Fig. 6d, 7a,c) and small enrichment in Th (Fig. 7a,d). εNd values (6.98-7.25) are

582   comparable to those of the basalts.

583   Boninites show a strong depletion in rare earth elements (Fig. 6a) and Ti (Fig. 7b), but

584   enrichment in Th and V (Fig. 7a,b). There are no Nd isotope measurements on these rocks.

585   There are no clues for high-pressure melting of slab lithologies (i.e. in the garnet stability

586   field, which would result in HREE-depleted adakitic magmas; e.g. Martin, 1999).

587   This set of data advocates for several partial melting events of a metasomatized supra-

588   subduction mantle source, with limited contamination by sediment-derived melts (at least

589   for the arc tholeiites and felsic rocks, likely involving more sediments in the boninites; Haase

590   et al., 2015; Ishikawa et al., 2005; Kusano et al., 2017). Hence the A_1 (core) unit of the Siah

591   Kuh seamount and the felsic rocks in the B unit represents the magmatic evolution of an

592   intraoceanic arc from an IAT to IAT/calc-alkaline-transitional felsic rocks and boninites. This

593   evolution is similar to what is currently recorded in intraoceanic arc systems, notably at the

594   initiation of subduction (e.g. Belgrano and Diamond, 2019; Hawkins et al., 1984; Pearce et

595   al., 1984; Stern and Bloomer, 1992).

596   Concordant zircons have been analyzed in a rhyolite from this event. They show a broad

597   range of ages (1823-85.7 Ma), but the youngest population (2 zircons) was dated at 87.0 ±

598   0.9 Ma, and is a plausible age for eruption, given the Campanian-Maastrichtian age of

599   overlying sediments proposed by Sabzehei (1974). The lowermost basalts (core of A unit

600   basaltic rocks) upon which this rhyolite was erupted should be somewhat older. Xenocrystic

601   zircons might originate from sediment melts possibly contaminating the mantle source

602   (although the contribution of sediment melts to the source of these rocks is very limited), or

603   they were more likely assimilated from the sub-arc crust during eruption.

604

605   **A MORB rejuvenation event**

606   In sharp contrast with the A_1 unit, lavas erupted above sediments (i.e. in the $A_{1'}$-A_2-A_3-A_4 and

607   B units) show no strong depletion in rare-earth elements (Fig. 6e), very limited-to-absent

608   HFSE negative anomalies (Fig. 6f) and no Th enrichment (Fig. 7a,d), i.e. no supra-subduction

609   signatures. They are in fact clustered in two trends (with some internal variability): the early

610   stage lavas show an E-MORB-like signature while the late stage is characteristic of N-MORB

611   (Fig. 6e,f and Fig. 7). A similar trend is observed in mafic rocks of the B unit (Fig. 6g,h), which

612   is thus likely to be a lateral equivalent of A, as suggested by the spatial association and the

613   correlation of lithologies. Clinopyroxene analyses confirm their mid-ocean ridge tholeiitic

614   signature (Fig. 9). The positive ϵNd of basalts (6.83 to 9.21; Fig. 8) is compatible with a

615   moderately depleted mantle source (Patchett, 1983). E-MORB and N-MORB lavas are

616   generated in modern oceans at mid-ocean ridges (Michael, 1995; Niu et al., 1999) and in

617   back-arc spreading centers (e.g. Stern et al., 1990). In the latter configuration, the

618   subduction signature is very variable, but its absence may be characteristic of a large

619   distance from the subduction and/or influence from a more primitive mantle (e.g. Lau Basin,

620   Volpe et al., 1988; Mariana back-arc, Pearce et al., 2005).

621   Anorthosite and gabbro in the B unit are two favorable lithologies for zircon dating. Both

622   rocks have similar ages within uncertainty around 77-78 Ma. The dated gabbro (#1532) has

623   REE and trace element profiles similar to N-MORB, and no obvious HFSE negative anomalies

624   (Fig. 6g,h). Its textural characteristics, reminiscent of cumulates (i.e. similar to some

625   observed on the Mid-Atlantic ridge, Tiezzi and Scott, 1980; depletion in REE and Eu positive

626   anomaly, Seifert et al., 1996), make it unsuitable for discrimination diagrams of figure 7.

627   Clinopyroxene analyses plot in the mid-ocean ridge tholeiite field (Fig. 9). This suggests that

628   this gabbro has a (likely N-) MORB affinity. An attempt to date zircons in basalts from top of

629   the B unit yielded a broad range of ages (1080-73.1 Ma), with a youngest population (two

630   zircons) giving a plausible eruption age of 73.7 ± 0.7 Ma that must be cautiously interpreted.

631   These Late Cretaceous ages are consistent with the relative chronology and the mapped

632   Upper Cretaceous sediments.

633 These data reveal a multistage magmatic history for the Siah Kuh seamount, which evolved

634 from arc tholeiite and boninite to calc-alkaline-transitional possibly until ~87 Ma, and later

635 experienced a distinct magmatic episode of E-to-N-MORB affinity, starting around 77.5 Ma

636 and possibly lasting until 73 Ma (Figs. 7a, 10).

637

638 ### *9.3.   Constraints on the nature and evolution of the underlying mantle*

639 Mantle rocks found in the Siah Kuh unit are mainly serpentinized dunites (A unit) and

640 cumulates (B unit). The high Cr# of spinels are characteristic of a depleted mantle (Dick and

641 Bullen, 1984; Moll et al., 2007). However, a second generation of Cr-richer spinel in a dunite

642 of the A unit might have formed by impregnation of the mantle by boninitic melts during

643 island arc volcanism (e.g. Barnes and Roeder, 2001).

644 The restricted spread of the εNd_i values accross all magmatic rocks analyzed suggest the

645 melting of a mantle source without a significant contribution from sediment melts (<1%), in

646 particular during the arc stage, when it is most expected (e.g. Zamboni et al., 2016). This

647 signature might however exist in boninites (not analyzed for Nd isotopes) that show a

648 significant Th enrichment. Hence, εNd_i values around 6-10 likely reflect the composition of a

649 slightly heterogeneous mantle that was not strongly contaminated by sediments during the

650 subduction responsible for arc formation. These values are very similar to those of other

651 regional ophiolites (Oman, Godard et al., 2006; Neyriz, Moghadam et al., 2014b; Nain-Baft,

652 Moghadam et al., 2013c), and are comparable with the abnormal modern Indian Ocean

653 MORB (likely refertilized by old subductions; Dupré and Allègre, 1983; Xu and Castillo, 2004).

654 $\varepsilon Hf(t)$ values of zircons are in majority positive (2 values are negative), around 14 for gabbro

655 and 9 for plagiogranite, which points to partially-depleted mantle sources with some

656 heterogeneity.

657 The evolution from supra-subduction to MORB signatures is opposite to what is observed in

658 many other ophiolites (e.g. Oman, Godard et al., 2003, Albania, Dilek et al., 2008), commonly

659 explained by progressive contamination of the mantle by subduction-derived fluids and

660 melts (occurring in ~1 My, Rioux et al., 2013). Instead, our observations are reminiscent of

661 longer-term processes (~10 My) occurring in modern arc-back-arc systems, such as the

662 Marianas: while the arc itself has a strong supra-subduction signature, back-arc lavas only

663 show a limited subduction component, due to the upwelling of uncontaminated mantle

664 (Pearce et al., 2005). The dissipation of the subduction signature could also be explained by

665 the end of subduction and the replacement of the underlying mantle facilitated by fast

666 horizontal asthenospheric flow (e.g. Faccenna et al., 2014).

667 The transition from E-MORB to N-MORB lavas (Fig 10) during the rejuvenation event might

668 be linked with (1) initial heterogeneity of the mantle, (2) a progressive depletion of an

669 initially enriched mantle source due to melt extraction, or (3) changes in the fusion rate of a

670 depleted mantle source. E-MORB lavas are usually thought to stem from plume enrichment

671 of the mantle or assimilation of formerly erupted lavas (e.g. Hémond et al., 2006). The

672 generation of N-MORB lavas could then result from a progressive depletion of this mantle

673 wedge due to melt extraction. An alternative way to form N-MORB lavas after E-MORB

674 basalts from the same depleted mantle source would merely require an increase of the

675 fusion rate by a few percents. However, this process would not explain the variability of the

676 Nb/Yb and Th/Yb ratios as well as the variability of zircon εHf(t) values and whole rock εNd

677 values, that require some heterogeneity in the underlying mantle. The Late Permian T_{DM} age

678 of zircons in gabbro might relate to the fusion of a mantle depleted during the Late Permian,

679 which corresponds to widespread magmatism on both sides of the Neotethys (potentially

680 plume-related, Ghasemi et al., 2002; Lapierre, 2004). Older (~550 Ma) T_{DM} in the anorthosite

681 could however relate to crustal contamination.

682 Finally, the presence of old zircons xenocrysts (200 Ma to 1.7 Ga) in Siah Kuh magmatic

683 rocks as well as granitoid xenoliths in the Siah Kuh volcanics (2-3-cm-long angular granitic-

684 to-granodioritic enclaves according to Sabzehei (1974) – though never observed in our

685 study) might reflect the nature of the sub-arc crust, partially assimilated during the ascent of

686 magma, or subducted sediments in the source (although this hypothesis is less likely given

687 the very limited contribution of sediments to the source). The ages of these zircons indeed

688 correspond to magmatic events recorded in the continental margins of the Neotethys

689 (Ahmadipour et al., 2003; Ghasemi et al., 2002; Moghadam et al., 2017).

690

691 ***9.4.   Geodynamic reconstructions of the Neotethys realm***

692   9.4.1. Chronological overview

693 The regional record of processes described below is detailed in Table 2.

694 **Initial rifting and early spreading history (Permian to Jurassic)**

695 In the Siah Kuh region, the magmatic history associated with rifting and early spreading of

696 the Neotethys is relatively well preserved in the Sikhoran complex: Late Permian to Late

697 Triassic gabbroic complexes have enriched to depleted tholeiitic signatures, with some
698 crustal contamination (Ahmadipour et al., 2003), and partially intrude the overlying
699 metamorphics. The end of high temperature metamorphism and anatexy of Sargaz-Abshur
700 sediments around 200 Ma (Early Jurassic; Ghasemi et al., 2002) are coeval with the sealing of
701 both igneous and metamorphic rocks by Lower Jurassic unmetamorphosed sediments
702 (Sabzehei, 1974). The Sikhoran complex would thus correspond to a Jurassic Ocean-
703 Continent Transition (e.g. Péron-Pinvidic and Manatschal, 2009) on the Northern Side of the
704 Neotethys. Equivalents would be the Bajgan-Durkan complex and the ultramafic Sorkhband-
705 Rudan massif (Delavari et al., 2016; Hunziker et al., 2015; McCall, 1997). Some of the rifting
706 history is recorded throughout Zagros and in Oman by the association of the Upper Triassic
707 to "Mid"-Cretaceous deep sediments (grabens) and shallow sediments, the latter being
708 described as allochtons or "Exotics" (Gharib and De Wever, 2010; Jannessary and
709 Whitechurch, 2008; Ricou, 1974; Ricou et al., 1977; Searle and Graham, 1982; Wrobel-
710 Daveau et al., 2010). Triassic to Liassic alkaline lavas (Ricou, 1974; Saccani et al., 2013;
711 Searle, 1980; Whitechurch et al., 2013) are precursors to Liassic volcanic sequences with E-
712 MORB affinities (although rarely exposed, e.g. Moghadam et al., 2017, 2013b; Searle, 1980).

713

714 **Subduction: arc development at the northern margin (Jurassic-Oligocene) and Cretaceous-**
715 **Paleocene back-arcs**
716 The structure of the Zagros suture zone suggests a strong inheritance from northward
717 subduction of the Neotethys/Arabian Plate below Iran (e.g. Agard et al., 2011), yet the
718 timing of subduction initiation is not well-constrained. Abundant subduction-related
719 magmatism has been associated with this subduction (Berberian and Berberian, 1981;
720 Omrani et al., 2008 and references therein). Although Early to Mid-Jurassic calk-alkaline
721 magmatism (e.g. Jafari et al., 2018; Shahbazi et al., 2010) suggests subduction initiation
722 during the Early Jurassic (see also the compilation of Hassanzadeh and Wernicke, 2016; their
723 figure 7), this interpretation is challenged by some authors, who outline that subduction
724 signatures could be related to crustal contamination (Azizi and Stern, 2019; Barbarin, 1999;
725 Hunziker et al., 2015). Instead, these authors propose an inception of subduction during Late
726 Cretaceous, which is however inconsistent with the recovery of 'mid' Cretaceous blueschists
727 made of Neotethyan seafloor in Zagros and Makran (as early as 120 Ma in Zagros, Agard et
728 al., 2006; Moghadam et al., 2017; and 100 Ma in Makran, Delaloye and Desmons, 1980), and

729 with Zagros eclogites possibly formed during Neotethyan subduction (with ages ~185-170

730 Ma, Davoudian et al., 2008, 2016).

731 Extension and spreading interpreted as back-arc in the Eurasian upper plate (Nain-Baft,

732 Sistan and Sabzevar basins), which started during Albian/Aptian (~125-100 Ma; Babazadeh

733 and de Wever, 2004; Moghadam et al., 2014a, 2009; Rossetti et al., 2010; Zarrinkoub et al.,

734 2012), also require that subduction started at least during Early Cretaceous.

735 Arc magmatism was recorded continuously in Southern Iran, in the Sanandaj-Sirjan zone

736 (until the Late Cretaceous; Jafari et al., 2018), the Kermanshah arc (Paleocene-Eocene;

737 Whitechurch et al., 2013), and the Urumieh-Dokhtar magmatic arc (post-Eocene; Omrani et

738 al., 2008).

739

740 **Late Cretaceous compressional event**

741 A main feature of the Neotethys is the intra-oceanic subduction that started at the end of

742 the Early Cretaceous in various areas (e.g. Oman, Neyriz, Turkey; Table 2), leading to the

743 emplacement of supra-subduction ophiolites and metamorphic soles (e.g. Hacker et al.,

744 1996).

745 Rocks from the core of the Siah Kuh seamount are very similar to those from the V2 stage in

746 the Semail ophiolite, in particular arc tholeiites and boninites (Alabaster et al., 1982;

747 Belgrano and Diamond, 2019; Godard et al., 2003; Ishikawa et al., 2005). This V2 event,

748 dated between 96.4 and 95.5 Ma (Rioux et al., 2013, 2012) is older than what is dated in Siah

749 Kuh. However, felsic intrusives in the Semail ophiolite have been dated between 90 and 85

750 Ma (Gnos and Peters, 1993; Lippard et al., 1986; Searle, 1980) and could correspond to the

751 felsic rocks in Siah Kuh. The few My delay between forearc magmatism (arc tholeiites and

752 boninites) in Oman and intra-oceanic arc magmatism (felsic rocks) recorded in Oman (and

753 potentially in the Siah Kuh unit) corresponds to the time required for the transition between

754 forearc and arc signatures (7-8 Myr in the Bonin arc; Ishizuka et al.,2011). The Neyriz and

755 Kermanshah ophiolitic complexes in Zagros potentially record similar processes (Babaie et

756 al., 2006, 2001; Delaloye and Desmons, 1980; Jannessary, 2003; Lanphere and Pamić, 1983;

757 Monsef et al., 2018a; Whitechurch et al., 2013).

758 Subduction initiation was linked with a compressive event (Agard et al., 2007, 2014)

759 responsible for the exhumation of blueschists all along the Neotethys from Turkey to the

760 Western Himalayas (Monié and Agard, 2009), as well as initiation of subduction within back-

761 arcs (e.g. Sabzevar: Rossetti et al., 2010; Sistan: Bonnet et al., 2018).

762 While arc magmatism is only subordinate in Oman, the Siah Kuh seamount core (A_1 unit),

763 formed around 87 Ma, may represent the arc products of this southern, intra-oceanic

764 subduction (see further discussion below).

765

766 **Evidence for a second Late Cretaceous spreading phase**

767 This study reports a Late Cretaceous MORB-type magmatic event in the Neotethys (i.e., B

768 unit and magmatic rejuvenation in A unit). In the Kermanshah ophiolite, a magmatic event at

769 ~79 Ma (Ao et al., 2016) was likely associated with a slow-spreading event (Wrobel-Daveau

770 et al., 2010). E-MORB dykes dated at ~81 and ~76 Ma in the Sikhoran complex (Ahmadipour

771 et al., 2003; Ghasemi et al., 2002) could also correspond to this magmatic event. In

772 comparison, an arc-related magmatic phase is recorded during the Late Cretaceous in the

773 Nain-Baft-North Makran ophiolites (Kananian et al., 2001; Monsef et al., 2018b).

774 The magmatic evolution observed in the Siah Kuh seamount hints to the change from an arc

775 to back-arc-like setting, and its possible original location in the Neotethys is therefore

776 discussed below.

777

778   9.4.2. Where was the arc?

779

780 The Siah Kuh seamount is presently sandwiched within the Zagros suture zone and domed

781 below other exposures of Zagros blueschists and of the Sikhoran complex (e.g. Agard et al.,

782 2006; Angiboust et al., 2016). Although challenged by some authors (e.g. Moghadam and

783 Stern, 2015), there is generally a consensus on the existence of two north-dipping

784 subduction zones within the Neotethys (e.g. Coleman, 1981; Searle and Cox, 1999; Rossetti

785 et al., 2010; Agard et al., 2011): (1) the long-lived North-Neotethys subduction zone initiated

786 during the Jurassic and lasting until Eocene, and (2) the short-lived South Neotethys

787 subduction zone initiated in mid-Cretaceous times and terminated by the Late Cretaceous

788 with the continental subduction of the Arabian platform (Agard et al., 2010; Searle et al.,

789 2004).

790 Geochemical evidence suggest that Siah Kuh formed in an intraoceanic forearc/arc setting,

791 and later evolved in a back-arc setting. Whether this occurred in the upper plate of

792   subduction (1) or (2) is unclear. We hereafter discuss two different scenarii featured in figure

793   12b and 12c.

794

795   **Hypothesis 1: Arc of the Southern Intra-Neotethys Subduction**

796   Most of the magmatic activity documented in the Southern Neotethys (e.g. Neyriz, Oman)

797   occurred around 95 Ma (e.g. Monsef et al., 2018a; Rioux et al., 2012; see Table 2). The 87

798   Ma age recorded within Siah Kuh is approximately 10 Ma younger than supra-subduction

799   magmatism. At this time, the Semail ophiolite underwent a ~140-150° clockwise rotation

800   and recorded alkaline magmatism (Morris et al., 2016; Umino, 2012; van Hinsbergen et al.,

801   2019). However, subduction had not ended yet (as shown by later subduction and blueschist

802   to eclogite metamorphism of the Arabian margin; e.g. El Shazly et al., 2001; Searle et al.,

803   2004; Yamato et al., 2007) and partial melting may have occurred in the mantle north of the

804   Semail ophiolite (Fig. 12b). Resulting magmas would probably be erupted on early Mesozoic

805   oceanic crust, possibly in the presence of extensional allochtons similar to those of the

806   Sargaz-Abshur complex. The development of an arc system more mature than in Oman (i.e.,

807   including true calc-alkaline magmas) could be favored by deeper and stronger hydration of

808   the mantle wedge.

809   The ~78 Ma event recorded in Siah Kuh corresponds to the time when continental rocks

810   start to be exhumed (El Shazly et al., 2001; Yamato et al., 2007). Resistance to the

811   convergence and subduction of the Arabian platform, combined with the slab pull generated

812   by the deeper oceanic slab could induce slab roll back, possibly followed by slab break off (a

813   deep slab was imaged by van der Meer et al., 2018). This process, modeled by Chemenda et

814   al. (1996), may have generated back-arc extension in the upper plate. An asthenospheric

815   window would also allow the influx of heat as well as enriched mantle that could form the

816   MORB lavas. If the Siah Kuh unit was located in an arc/back-arc of the Southern Neotethys

817   Subduction, it would belong to the lower plate of the Northern Neotethys Subduction and

818   get subducted lately (i.e. close to collision, for example during the late Paleocene-Eocene)

819   along with remnants of the Early Mesozoic seafloor. This hypothesis easily explains its

820   underplating beneath the Ashin and Seghin blueschist facies units (Fig. 12b; Agard et al.,

821   2006a; Angiboust et al., 2016a).

822

823   **Hypothesis 2: Arc of the Northern Neotethys Subduction?**

824 The present position of the Siah Kuh unit below the other Zagros blueschists (Agard et al.,
825 2006) and sequential accretion outlined by Angiboust et al. (2016) make it difficult to
826 reconcile with a Northern Neotethys subduction zone (see Fig. 12b,c). The main argument
827 for a genesis in this context is a possible genetic link between the Sikhoran-Sargaz-Abshur
828 complexes and the Siah Kuh seamount, as discussed above. No clear arc magmatism at 87
829 Ma is however described in the obducted ophiolites (Semail-Neyriz) or in the Sanandaj-Sirjan
830 zone surrounding the Siah Kuh unit. Genesis of Siah Kuh above the Northern Neotethys
831 subduction would require the existence of extensional allochtons similar to the Sargaz-
832 Abshur complex (to explain the zircon distribution). Formation above the Northern
833 Neotethys subduction could explain the Late Cretaceous E-MORB dykes within the Sikhoran
834 complex. Arc magmatism in Siah Kuh likely corresponds to a magmatic event recorded in
835 Makran by detrital zircons aged 90-85 Ma, interpreted by Mohammadi et al. (2017) and Burg
836 (2018) to result from arc magmatism on the Northern margin of the Neotethys. However,
837 detrital zircons aged 80-75 Ma are not particularly abundant in these studies.

838 In this configuration, subduction of the Siah Kuh seamount would require (1) initiation of a
839 new subduction zone to the north of the Northern Tethys Subduction or (2) a northward
840 migration of the subduction zone, for example through a splay fault (dotted line in Fig. 12c).
841 Initiation of a new subduction zone above a pre-existing one is observed in Southeastern
842 Taiwan, where a large portion of the forearc gets subducted (e.g. Malavieille et al., 2002).
843 Boutelier et al. (2003) suggested that subduction initiation would occur preferentially in the
844 back-arc. In this configuration, however, subduction of the largely intact Siah Kuh seamount
845 would require a huge mega-splay fault, much larger than the one observed in the Nankai
846 accretionary wedge (Park et al., 2002).

847

848 **10. Conclusion**

849 The Siah Kuh unit is a former seamount, now outcropping in the Zagros Suture Zone. It is
850 composed of two units separated by a major thrust, both of which record a comparable
851 magmatic and geodynamic history:

852   1) The seamount was built around 87 Ma in an intraoceanic forearc/arc setting and
853   witnesses increasing maturity and metasomatism of the mantle wedge through time.
854   2) A resumption of magmatism occurred around 78-73 Ma in a back-arc-like setting,
855   with a transition from enriched to depleted lavas.

856   3) The Siah Kuh seamount was later subducted below the Eurasian plate (meanwhile,
857   the B unit was thrust onto the A unit), at ~30 km depth, and thereafter exhumed (Fig.
858   12a).

859 Combining structural and geochemical data from other magmatic and metamorphic
860 episodes in the Iranian-Omanese Neotethys realm (Table 2), which was affected by two
861 subduction zones during the Late Cretaceous, we propose two possible tectono-magmatic
862 settings for the Siah Kuh seamount. This exceptional remnant might represent (1) an arc
863 located above the Southern Neotethys subduction zone (Fig. 12b), and would therefore
864 represent a non-obducted piece (and the 'missing arc') of the Oman ophiolite, or (2) an arc
865 to forearc domain at the Northern Margin of the Neotethys (Fig. 12c). We consider the first
866 hypothesis more likely (Fig. 12b).

867
868

876

877 **References:**
878 Agard, P., Jolivet, L., Vrielynck, B., Burov, E., Monié, P., 2007. Plate acceleration: The
879 obduction trigger? Earth and Planetary Science Letters 258, 428–441.
880 https://doi.org/10.1016/j.epsl.2007.04.002
881 Agard, P., Monié, P., Gerber, W., Omrani, J., Molinaro, M., Meyer, B., Labrousse, L.,
882 Vrielynck, B., Jolivet, L., Yamato, P., 2006. Transient, synobduction exhumation of Zagros
883 blueschists inferred from P-T, deformation, time, and kinematic constraints: Implications for
884 Neotethyan wedge dynamics. Journal of Geophysical Research 111, B11401.
885 https://doi.org/10.1029/2005JB004103
886 Agard, P., Omrani, J., Jolivet, L., Whitechurch, H., Vrielynck, B., Spakman, W., Monié, P.,
887 Meyer, B., Wortel, M.J.R., 2011. Zagros orogeny: a subduction-dominated process.
888 Geological Magazine 148, 692–725. https://doi.org/10.1017/S001675681100046X
889 Agard, P., Searle, M.P., Alsop, G.I., Dubacq, B., 2010. Crustal stacking and expulsion
890 tectonics during continental subduction: P-T deformation constraints from Oman. Tectonics
891 29. https://doi.org/10.1029/2010TC002669
892 Agard, P., Zuo, X., Funiciello, F., Bellahsen, N., Faccenna, C., Savva, D., 2014. Obduction:
893 Why, how and where. Clues from analog models. Earth and Planetary Science Letters 393,

894   132–145. https://doi.org/10.1016/j.epsl.2014.02.021

895   Ahmadipour, H., Sabzehei, M., Whitechurch, H., Rastad, E., Emami, M.H., 2003. Soghan
896   complex as an evidence for paleospreading center and mantle diapirism in Sanandaj-Sirjan
897   Zone (South-East Iran). Journal of Sciences, Islamic Republic of Iran 14, 157–172.

898   Alabaster, T., Pearce, J.A., Malpas, J., 1982. The volcanic stratigraphy and petrogenesis of the
899   Oman ophiolite complex. Contributions to Mineralogy and Petrology 81, 168–183.
900   https://doi.org/10.1007/BF00371294

901   Ali, S.A., Buckman, S., Aswad, K.J., Jones, B.G., Ismail, S.A., Nutman, A.P., 2012.
902   Recognition of Late Cretaceous Hasanbag ophiolite-arc rocks in the Kurdistan Region of the
903   Iraqi Zagros suture zone: A missing link in the paleogeography of the closing Neotethys
904   Ocean. Lithosphere 4, 395–410. https://doi.org/10.1130/L207.1

905   Andersen, T., 2002. Correction of common lead in U-Pb analyses that do not report204Pb.
906   Chemical Geology 192, 59–79. https://doi.org/10.1016/S0009-2541(02)00195-X

907   Angiboust, S., Agard, P., Glodny, J., Omrani, J., Oncken, O., 2016. Zagros blueschists:
908   Episodic underplating and long-lived cooling of a subduction zone. Earth and Planetary
909   Science Letters 443, 48–58. https://doi.org/10.1016/j.epsl.2016.03.017

910   Ao, S., Xiao, W., Khalatbari Jafari, M., Talebian, M., Chen, L., Wan, B., Ji, W., Zhang, Z.,
911   2016. U–Pb zircon ages, field geology and geochemistry of the Kermanshah ophiolite (Iran):
912   From continental rifting at 79 Ma to oceanic core complex at ca. 36 Ma in the southern Neo-
913   Tethys. Gondwana Research 31, 305–318. https://doi.org/10.1016/j.gr.2015.01.014

914   Arvin, M., Pan, Y., Dargahi, S., Malekizadeh, A., Babaei, A., 2007. Petrochemistry of the
915   Siah-Kuh granitoid stock southwest of Kerman, Iran: Implications for initiation of Neotethys
916   subduction. Journal of Asian Earth Sciences 30, 474–489.
917   https://doi.org/10.1016/j.jseaes.2007.01.001

918   Arvin, M., Robinson, P.T., 1994. The petrogenesis and tectonic setting of lavas from the Baft
919   Ophiolitic Mélange, southwest of Kerman, Iran. Canadian Journal of Earth Sciences 31, 824–
920   834. https://doi.org/10.1139/e94-076

921   Azizan, H., Naderi, N., Navazi, M., Poshtkuhi, M., Rashid, H., Abazari, Z., Haddadan, M.,
922   2007. Geological Map of Iran, 1 : 100000 series - Dolatabad.

923   Azizi, H., Stern, R.J., 2019. Jurassic igneous rocks of the central Sanandaj–Sirjan zone (Iran)
924   mark a propagating continental rift, not a magmatic arc. Terra Nova.
925   https://doi.org/10.1111/ter.12404

926   Babaie, H.A., Babaei, A., Ghazi, A.M., Arvin, M., 2006. Geochemical, [40]Ar/ [39]Ar age, and
927   isotopic data for crustal rocks of the Neyriz ophiolite, Iran. Canadian Journal of Earth
928   Sciences 43, 57–70. https://doi.org/10.1139/e05-111

929   Babaie, H.A., Ghazi, A.M., Babaei, A., La Tour, T.E., Hassanipak, A.A., 2001. Geochemistry
930   of arc volcanic rocks of the Zagros Crush Zone, Neyriz, Iran. Journal of Asian Earth Sciences
931   19, 61–76. https://doi.org/10.1016/S1367-9120(00)00012-2

932   Babazadeh, S.A., de Wever, P., 2004. Early Cretaceous radiolarian assemblages from
933   radiolarites in the Sistan Suture (eastern Iran). Geodiversitas 26, 185–206.

934   Bagheri, S., Stampfli, G.M., 2008. The Anarak, Jandaq and Posht-e-Badam metamorphic
935   complexes in central Iran: New geological data, relationships and tectonic implications.
936   Tectonophysics 451, 123–155. https://doi.org/10.1016/j.tecto.2007.11.047

937   Barbarin, B., 1999. A review of the relationships between granitoid types, their origins and
938   their geodynamic environments. Lithos 46, 605–626. https://doi.org/10.1016/S0024-
939   4937(98)00085-1

940   Barnes, S.J., Roeder, P.L., 2001. The Range of Spinel Compositions in Terrestrial Mafic and
941   Ultramafic Rocks. Journal of Petrology 42, 2279–2302.
942   https://doi.org/10.1093/petrology/42.12.2279

943   Barrier, E., Vrielynck, B., 2008. Palaeotectonic Maps of the Middle East: Late Maastrichtian.

944   Commission de la Carte Géologique du Monde Map 8.

945   Batiza, R., Vanko, D., 1984. Petrology of young Pacific Seamounts. Journal of Geophysical

946   Research 89, 11,211-235,260. https://doi.org/10.1029/JB089iB13p11235

947   Belgrano, T.M., Diamond, L.W., 2019. Subduction-zone contributions to axial volcanism in

948   the Oman–U.A.E. ophiolite. Lithosphere 11, 399–411. https://doi.org/10.1130/L1045.1

949   Berberian, F., Berberian, M., 1981. Tectono-plutonic episodes in Iran, in: Gupta, H.K.,

950   Delany, F.M. (Eds.), Geodynamics Series, Geodynamics Series. American Geophysical

951   Union, pp. 33–69.

952   Bonnet, G., Agard, P., Angiboust, S., Fournier, M., Omrani, J., 2019a. No large earthquakes

953   in fully exposed subducted seamount. Geology 47, 407–410.

954   https://doi.org/doi.org/10.1130/G45564.1

955   Bonnet, G., Agard, P., Angiboust, S., Monié, P., Fournier, M., Caron, B., Omrani, J., 2019b.

956   Structure and metamorphism of a subducted seamount (Zagros suture, Southern Iran).

957   Geosphere 15. https://doi.org/10.1130/GES02134.1.

958   Bonnet, G., Agard, P., Angiboust, S., Monié, P., Jentzer, M., Omrani, J., Whitechurch, H.,

959   Fournier, M., 2018. Tectonic slicing and mixing processes along the subduction interface: The

960   Sistan example (Eastern Iran). Lithos 310–311, 269–287.

961   https://doi.org/10.1016/j.lithos.2018.04.016

962   Boudier, F., Ceuleneer, G., Nicolas, A., 1988. Shear zones, thrusts and related magmatism in

963   the Oman ophiolite: Initiation of thrusting on an oceanic ridge. Tectonophysics 151, 275–296.

964   https://doi.org/10.1016/0040-1951(88)90249-1

965   Boutelier, D., Chemenda, A., Burg, J.-P., 2003. Subduction versus accretion of intra-oceanic

966   volcanic arcs: insight from thermo-mechanical analogue experiments. Earth and Planetary

967   Science Letters 212, 31–45. https://doi.org/10.1016/S0012-821X(03)00239-5

968   Bouvier, A., Vervoort, J.D., Patchett, P.J., 2008. The Lu–Hf and Sm–Nd isotopic composition

969   of CHUR: Constraints from unequilibrated chondrites and implications for the bulk

970   composition of terrestrial planets. Earth and Planetary Science Letters 273, 48–57.

971   https://doi.org/10.1016/j.epsl.2008.06.010

972   Briqueu, L., Bougault, H., Joron, J.L., Gbochimie, I.L. De, Cg, G., Sciences, U.E.R., Terre,

973   D., Bataillon, U.S.T.L.P.E., Montpellier, C., 1984. Quantification of Nb, Ta, Ti and V

974   anomalies in magmas associated with subduction zones: petrogenetic implications. Earth and

975   Planetary Science Letters 68, 297–308.

976   Burg, J.-P., 2018. Geology of the onshore Makran accretionary wedge: Synthesis and tectonic

977   interpretation. Earth-Science Reviews 185, 1210–1231.

978   https://doi.org/10.1016/j.earscirev.2018.09.011

979   Cann, J.R., 1970. Rb, Sr, Y, Zr and Nb in some ocean floor basaltic rocks. Earth and

980   Planetary Science Letters 10, 7–11. https://doi.org/10.1016/0012-821X(70)90058-0

981   Casey, J.F., Dewey, J.F., 1984. Initiation of subduction zones along transform and accreting

982   plate boundaries, triple-junction evolution, and forearc spreading centres—implications for

983   ophiolitic geology and obduction. Geological Society, London, Special Publications 13, 269–

984   290. https://doi.org/10.1144/GSL.SP.1984.013.01.22

985   Chemenda, A.I., Mattauer, M., Bokun, A.N., 1996. Continental subduction and a mechanism

986   for exhumation of high-pressure metamorphic rocks: new modelling and field data from

987   Oman. Earth and Planetary Science Letters 143, 173–182. https://doi.org/10.1016/0012-

988   821X(96)00123-9

989   Cloos, M., 1993. Lithospheric buoyancy and collisional orogenesis: subduction of oceanic

990   plateaus, continental margins, island arcs, spreading ridges, and seamounts. Geological

991   Society of America Bulletin 105, 715–737. https://doi.org/10.1130/0016-

992   7606(1993)105<0715:LBACOS>2.3.CO

993   Coleman, R.G., 1981. Tectonic setting for ophiolite obduction in Oman. Journal of

Geophysical Research 86, 2497–2508. https://doi.org/10.1029/JB086iB04p02497

Davoudian, A.R., Genser, J., Dachs, E., Shabanian, N., 2008. Petrology of eclogites from north of Shahrekord, Sanandaj-Sirjan Zone, Iran. Mineralogy and Petrology 92, 393–413. https://doi.org/10.1007/s00710-007-0204-6

Davoudian, A.R., Genser, J., Neubauer, F., Shabanian, N., 2016. ^{40}Ar/^{39}Ar mineral ages of eclogites from North Shahrekord in the Sanandaj–Sirjan Zone, Iran: Implications for the tectonic evolution of Zagros orogen. Gondwana Research 37, 216–240. https://doi.org/10.1016/j.gr.2016.05.013

Delaloye, M., Desmons, J., 1980. Ophiolites and melange terranes in Iran: A geochronological study and its paleotectonic implications. Tectonophysics 68, 83–111. https://doi.org/10.1016/0040-1951(80)90009-8

Delavari, M., Dolati, A., Marroni, M., Pandolfi, L., Saccani, E., 2016. Association of MORB and SSZ Ophiolites Along the Shear Zone Between Coloured Mélange and Bajgan Complexes (north Makran, Iran): Evidence from the Sorkhband Area. Ofioliti. https://doi.org/10.4454/ofioliti.v41i1.440

Dick, H.J.B., Bullen, T., 1984. Chromian spinel as a petrogenetic indicator in abyssal and alpine-type peridotites and spatially associated lavas. Contributions to Mineralogy and Petrology 86, 54–76. https://doi.org/10.1007/BF00373711

Dilek, Y., Furnes, H., Shallo, M., 2008. Geochemistry of the Jurassic Mirdita Ophiolite (Albania) and the MORB to SSZ evolution of a marginal basin oceanic crust. Lithos 100, 174–209. https://doi.org/10.1016/j.lithos.2007.06.026

Droop, G.T.R., 1987. A General Equation for Estimating Fe^{3+} Concentrations in Ferromagnesian Silicates and Oxides from Microprobe Analyses, Using Stoichiometric Criteria. Mineralogical Magazine 51, 431–435. https://doi.org/10.1180/minmag.1987.051.361.10

Dupré, B., Allègre, C.J., 1983. Pb–Sr isotope variation in Indian Ocean basalts and mixing phenomena. Nature 303, 142–146. https://doi.org/10.1038/303142a0

El Shazly, A.E.-D.K., Bröcker, M., Hacker, B.R., Calvert, A.J., 2001. Formation and exhumation of blueschists and eclogites from NE Oman: new perspectives from Rb-Sr and ^{40}Ar/^{39}Ar dating. Journal of Metamorphic Geology 19, 233–248. https://doi.org/10.1046/j.1525-1314.2001.00309.x

Faccenna, C., Becker, T.W., Auer, L., Billi, A., Boschi, L., Brun, J.P., Capitanio, F.A., Funiciello, F., Horvàth, F., Jolivet, L., Piromallo, C., Royden, L., Rossetti, F., Serpelloni, E., 2014. Mantle dynamics in the Mediterranean. Reviews of Geophysics 52, 283–332. https://doi.org/10.1002/2013RG000444

Frey, F.A., Weis, D., 1995. Temporal evolution of the kerguelen plume: Geochemical evidence from 38 to 82 ma lavas forming the Ninetyeast ridge. Contributions to Mineralogy and Petrology 121, 12–28. https://doi.org/10.1007/s004100050087

Gansser, A., 1960. Ausseralpine Ophiolothprobleme. Eclogae Geologicae Helvetiae 52, 659–680.

Gao, J., John, T., Klemd, R., Xiong, X., 2007. Mobilization of Ti–Nb–Ta during subduction: Evidence from rutile-bearing dehydration segregations and veins hosted in eclogite, Tianshan, NW China. Geochimica et Cosmochimica Acta 71, 4974–4996. https://doi.org/10.1016/j.gca.2007.07.027

Gharib, F., De Wever, P., 2010. Radiolaires Mésozoïques de la formation de Kermanshah (Iran). Comptes Rendus Palevol 9, 209–219. https://doi.org/10.1016/j.crpv.2010.06.003

Ghasemi, A., Talbot, C.J., 2006. A new tectonic scenario for the Sanandaj-Sirjan Zone (Iran). Journal of Asian Earth Sciences 26, 683–693. https://doi.org/10.1016/j.jseaes.2005.01.003

Ghasemi, H., Juteau, T., Bellon, H., Sabzehei, M., Whitechurch, H., Ricou, L.-E., 2002. The mafic–ultramafic complex of Sikhoran (central Iran): a polygenetic ophiolite complex.

1044   Comptes Rendus Geoscience 334, 431–438. https://doi.org/10.1016/S1631-0713(02)01770-4

1045   Ghazi, A.M., Hassanipak, A.A., Mahoney, J.J., Duncan, R.A., 2004. Geochemical

1046   characteristics, $^{40}Ar–^{39}Ar$ ages and original tectonic setting of the Band-e-Zeyarat/Dar Anar

1047   ophiolite, Makran accretionary prism, S.E. Iran. Tectonophysics 393, 175–196.

1048   https://doi.org/10.1016/j.tecto.2004.07.035

1049   Gillis, K.M., 1995. Controls on hydrothermal alteration in a section of fast-spreading oceanic

1050   crust. Earth and Planetary Science Letters 134, 473–489. https://doi.org/10.1016/0012-

1051   821X(95)00137-2

1052   Gnos, E., Peters, T., 1993. K-Ar ages of the metamorphic sole of the Semail Ophiolite:

1053   implications for ophiolite cooling history. Contributions to Mineralogy and Petrology 113,

1054   325–332. https://doi.org/10.1007/BF00286925

1055   Godárd, M., Bosch, D., Einaudi, F., 2006. A MORB source for low-Ti magmatism in the

1056   Semail ophiolite. Chemical Geology 234, 58–78.

1057   https://doi.org/10.1016/j.chemgeo.2006.04.005

1058   Godárd, M., Dautria, J.M., Perrin, M., 2003. Geochemical variability of the Oman ophiolite

1059   lavas: Relationship with spatial distribution and paleomagnetic directions. Geochemistry,

1060   Geophysics, Geosystems 4. https://doi.org/10.1029/2002GC000452

1061   Goodenough, K.M., Styles, M.T., Schofield, D., Thomas, R.J., Crowley, Q.C., Lilly, R.M.,

1062   McKervey, J., Stephenson, D., Carney, J.N., 2010. Architecture of the Oman–UAE ophiolite:

1063   evidence for a multi-phase magmatic history. Arabian Journal of Geosciences 3, 439–458.

1064   https://doi.org/10.1007/s12517-010-0177-3

1065   Guilmette, C., Smit, M.A., van Hinsbergen, D.J.J., Gürer, D., Corfu, F., Charette, B.,

1066   Maffione, M., Rabeau, O., Savard, D., 2018. Forced subduction initiation recorded in the sole

1067   and crust of the Semail Ophiolite of Oman. Nature Geoscience 11, 688–695.

1068   https://doi.org/10.1038/s41561-018-0209-2

1069   Haase, K.M., Freund, S., Koepke, J., Hauff, F., Erdmann, M., 2015. Melts of sediments in the

1070   mantle wedge of the Oman ophiolite. Geology 43, 275–278. https://doi.org/10.1130/G36451.1

1071   Hacker, B.R., Mosenfelder, J.L., Gnos, E., 1996. Rapid emplacement of the Oman ophiolite:

1072   Thermal and geochronologic constraints. Tectonics 15, 1230–1247.

1073   https://doi.org/10.1029/96TC01973

1074   Hassanzadeh, J., Wernicke, B.P., 2016. The Neotethyan Sanandaj-Sirjan zone of Iran as an

1075   archetype for passive margin-arc transitions. Tectonics 35, 586–621.

1076   https://doi.org/10.1002/2015TC003926

1077   Hastie, A.R., Kerr, A.C., Pearce, J.A., Mitchell, S.F., 2007. Classification of Altered Volcanic

1078   Island Arc Rocks using Immobile Trace Elements: Development of the Th–Co Discrimination

1079   Diagram. Journal of Petrology 48, 2341–2357. https://doi.org/10.1093/petrology/egm062

1080   Hauff, F., Hoernle, K., Schmidt, A., 2003. Sr-Nd-Pb composition of Mesozoic Pacific oceanic

1081   crust (Site 1149 and 801, ODP Leg 185): Implications for alteration of ocean crust and the

1082   input into the Izu-Bonin-Mariana subduction system: SR-ND-PB COMPOSITION OF

1083   MESOZOIC PACIFIC. Geochem. Geophys. Geosyst. 4.

1084   https://doi.org/10.1029/2002GC000421

1085   Hauff, F., Hoernle, K., Schmincke, H.-U., Werner, R., 1997. A Mid Cretaceous origin for the

1086   Galápagos hotspot: volcanological, petrological and geochemical evidence from Costa Rican

1087   oceanic crustal segments. Geologische Rundschau 86, 141–155.

1088   https://doi.org/10.1007/PL00009938

1089   Hawkins, J.W., Bloomer, S.H., Evans, C.A., Melchior, J.T., 1984. Evolution of intra-oceanic

1090   arc-trench systems. Tectonophysics 102, 175–205. https://doi.org/10.1016/0040-

1091   1951(84)90013-1

1092   Hémond, C., Hofmann, A.W., Vlastélic, I., Nauret, F., 2006. Origin of MORB enrichment

1093   and relative trace element compatibilities along the Mid-Atlantic Ridge between 10° and

1094 24°N. Geochemistry, Geophysics, Geosystems 7, n/a-n/a.
1095 https://doi.org/10.1029/2006GC001317
1096 Hochstaedter, A., Gill, J., Peters, R., Broughton, P., Holden, P., Taylor, B., 2001. Across-arc
1097 geochemical trends in the Izu-Bonin arc: Contributions from the subducting slab.
1098 Geochemistry, Geophysics, Geosystems 2. https://doi.org/10.1029/2000GC000105
1099 Humphris, S.E., Thompson, G., 1978. Trace element mobility during hydrothermal alteration
1100 of oceanic basalts. Geochimica et Cosmochimica Acta 42, 127–136.
1101 https://doi.org/10.1016/0016-7037(78)90222-3
1102 Hunziker, D., Burg, J.-P., Bouilhol, P., von Quadt, A., 2015. Jurassic rifting at the Eurasian
1103 Tethys margin: Geochemical and geochronological constraints from granitoids of North
1104 Makran, southeastern Iran. Tectonics 34, 571–593. https://doi.org/10.1002/2014TC003768
1105 Hunziker, D., Burg, J.-P., Moulas, E., Reusser, E., Omrani, J., 2017. Formation and
1106 preservation of fresh lawsonite: Geothermobarometry of the North Makran Blueschists,
1107 southeast Iran. Journal of Metamorphic Geology 35, 871–895.
1108 https://doi.org/10.1111/jmg.12259
1109 Ishikawa, T., Fujisawa, S., Nagaishi, K., Masuda, T., 2005. Trace element characteristics of
1110 the fluid liberated from amphibolite-facies slab: Inference from the metamorphic sole beneath
1111 the Oman ophiolite and implication for boninite genesis. Earth and Planetary Science Letters
1112 240, 355–377. https://doi.org/10.1016/j.epsl.2005.09.049
1113 Ishikawa, T., Nagaishi, K., Umino, S., 2002. Boninitic volcanism in the Oman ophiolite:
1114 Implications for thermal condition during transition from spreading ridge to arc. Geology 30,
1115 899–902. https://doi.org/10.1130/0091-7613(2002)030<0899:BVITOO>2.0.CO;2
1116 Ishizuka, O., Tani, K., Reagan, M.K., Kanayama, K., Umino, S., Harigane, Y., Sakamoto, I.,
1117 Miyajima, Y., Yuasa, M., Dunkley, D.J., 2011. The timescales of subduction initiation and
1118 subsequent evolution of an oceanic island arc. Earth and Planetary Science Letters 306, 229–
1119 240. https://doi.org/10.1016/j.epsl.2011.04.006
1120 Jafari, A., Fazlnia, A., Jamei, S., 2018. Geochemistry, petrology and geodynamic setting of
1121 the Urumieh plutonic complex, Sanandaj–Sirjan zone, NW Iran: New implication for Arabian
1122 and Central Iranian plate collision. Journal of African Earth Sciences 139, 421–439.
1123 https://doi.org/10.1016/j.jafrearsci.2017.11.039
1124 Jannessary, M.R., 2003. Les ophiolites de Neyriz (Sud de l'Iran) : Naissance d'une dorsale en
1125 pied de marge continentale (étude des structures internes, de la fabrique du manteau, et de
1126 l'évolution pétro-géochimique des magmas) (PhD thesis). Université Louis Pasteur,
1127 Strasbourg.
1128 Jannessary, M.R., Whitechurch, H., 2008. The birth of an oceanic crust at the foot of Gond-
1129 wana margin (Neyriz ophiolite, Iran). Geosciences 17, 41–48.
1130 John, T., Scherer, E.E., Schenk, V., Herms, P., Halama, R., Garbe-Schönberg, C.-D., 2010.
1131 Subducted seamounts in an eclogite-facies ophiolite sequence: the Andean Raspas Complex,
1132 SW Ecuador. Contributions to Mineralogy and Petrology 159, 265–284.
1133 https://doi.org/10.1007/s00410-009-0427-0
1134 Kananian, A., Juteau, T., Bellon, H., Darvishzadeh, A., Sabzehi, M., Whitechurch, H., Ricou,
1135 L.-E., 2001. The ophiolite massif of Kahnuj (western Makran, southern Iran): new geological
1136 and geochronological data. Comptes Rendus de l'Académie des Sciences - Series IIA - Earth
1137 and Planetary Science 332, 543–552. https://doi.org/10.1016/S1251-8050(01)01574-9
1138 Kawahata, H., Nohara, M., Ishizuka, H., Hasebe, S., Chiba, H., 2001. Sr isotope geochemistry
1139 and hydrothermal alteration of the Oman ophiolite. J. Geophys. Res. 106, 11083–11099.
1140 https://doi.org/10.1029/2000JB900456
1141 Khalatbari-Jafari, M., Juteau, T., Bellon, H., Whitechurch, H., Cotten, J., Emami, H., 2004.
1142 New geological, geochronological and geochemical investigations on the Khoy ophiolites and
1143 related formations, NW Iran. Journal of Asian Earth Sciences 23, 507–535.

https://doi.org/10.1016/j.jseaes.2003.07.005

König, S., Münker, C., Schuth, S., Luguet, A., Hoffmann, J.E., Kuduon, J., 2010. Boninites as windows into trace element mobility in subduction zones. Geochimica et Cosmochimica Acta 74, 684–704. https://doi.org/10.1016/j.gca.2009.10.011

Kusano, Y., Hayashi, M., Adachi, Y., Umino, S., Miyashita, S., 2014. Evolution of volcanism and magmatism during initial arc stage: constraints on the tectonic setting of the Oman Ophiolite. Geological Society, London, Special Publications 392, 177–193. https://doi.org/10.1144/SP392.9

Kusano, Y., Umino, S., Shinjo, R., Ikei, A., Adachi, Y., Miyashita, S., Arai, S., 2017. Contribution of slab-derived fluid and sedimentary melt in the incipient arc magmas with development of the paleo-arc in the Oman Ophiolite. Chemical Geology 449, 206–225. https://doi.org/10.1016/j.chemgeo.2016.12.012

Lachize, M., Lorand, J.P., Juteau, T., 1996. Calc-alkaline differentiation trend in the plutonic sequence of the Wadi Haymiliyah section, Haylayn massif, Semail ophiolite, Oman. Lithos 38, 207–232. https://doi.org/10.1016/0024-4937(96)00009-6

Lanphere, M.A., Pamić, J., 1983. Ages and tectonic setting of ophiolite from the Neyriz area, southeast Zagros Range, Iran. Tectonophysics 96, 245–256. https://doi.org/10.1016/0040-1951(83)90220-2

Lapierre, H., 2004. The Tethyan plume: geochemical diversity of Middle Permian basalts from the Oman rifted margin. Lithos 74, 167–198. https://doi.org/10.1016/j.lithos.2004.02.006

Leterrier, J., Maury, R.C., Thonon, P., Girard, D., Marchal, M., 1982. Clinopyroxene composition as a method of identification of the magmatic affinities of paleo-volcanic series. Science 59, 139–154.

Lippard, S.J., Shelton, A.W., Gass, I.G., 1986. The ophiolite of Northern Oman, The Geological Society. ed.

Liu, Y., Gao, S., Hu, Z., Gao, C., Zong, K., Wang, D., 2010. Continental and Oceanic Crust Recycling-induced Melt-Peridotite Interactions in the Trans-North China Orogen: U-Pb Dating, Hf Isotopes and Trace Elements in Zircons from Mantle Xenoliths. Journal of Petrology 51, 537–571. https://doi.org/10.1093/petrology/egp082

Liu, Y., Hu, Z., Gao, S., Günther, D., Xu, J., Gao, C., Chen, H., 2008. In situ analysis of major and trace elements of anhydrous minerals by LA-ICP-MS without applying an internal standard. Chemical Geology 257, 34–43. https://doi.org/10.1016/j.chemgeo.2008.08.004

Ludwig, K.R., 2001. Users Manual for Isoplot/Ex.: A Geochronological Toolkit for Microsoft Excel.

MacPherson, G.T., 1983. The Snow Mountain Volcanic Complex: an on-land seamount in the Franciscan Terrain, California. Journal of Geology 91, 73–92.

Madjidi, B., Berberian, M., Hushmandzadeh, A., Nowgole-Sadat, M.A.A., Sabzehei, M., Alavi-Tehrani, N., Azizan, H., Nazemzadeh, M., Roshan ravan-H, J., Afaghe, A., Afsharianzadeh, A.M., Dehhaghe, F., Ghomashi, A., 1993. Geological Map of Iran, 1 : 250000 series - Haji Abad.

Malavieille, J., Lallemand, S.E., Dominguez, S., Deschamps, A., Lu, C.-Y., Liu, C.-S., Schnuerle, P., Angelier, J., Collot, J.Y., Deffontaines, B., Fournier, M., Hsu, S.K., Le Formal, J.P., Liu, S.Y., Sibuet, J.C., Thareau, N., Wang, F., the ACT (Active Collision in Taiwan) Scientific Crew, 2002. Arc-continent collision in Taiwan: New marine observations and tectonic evolution, in: Special Paper 358: Geology and Geophysics of an Arc-Continent Collision, Taiwan. Geological Society of America, pp. 187–211. https://doi.org/10.1130/0-8137-2358-2.187

Martin, H., 1999. Adakitic magmas: Modern analogues of Archaean granitoids. Lithos 46, 411–429. https://doi.org/10.1016/S0024-4937(98)00076-0

McCall, G.J.H., 1997. The geotectonic history of the Makran and adjacent areas of southern Iran. Journal of Asian Earth Sciences 15, 517–531. https://doi.org/10.1016/S0743-9547(97)00032-9

McCulloch, M.T., Gregory, R.T., Wasserburg, G.J., Taylor, H.P., 1981. Sm-Nd, Rb-Sr, and $^{18}O/^{16}O$ isotopic systematics in an oceanic crustal section: Evidence from the Samail Ophiolite. Journal of Geophysical Research: Solid Earth 86, 2721–2735. https://doi.org/10.1029/JB086iB04p02721

Michael, P., 1995. Regionally distinctive sources of depleted MORB: Evidence from trace elements and H_2O. Earth and Planetary Science Letters 131, 301–320. https://doi.org/10.1016/0012-821X(95)00023-6

Moghadam, H.S., Bröcker, M., Griffin, W.L., Li, X.H., Chen, R.-X., O'Reilly, S.Y., 2017. Subduction, high-P metamorphism, and collision fingerprints in South Iran: Constraints from zircon U-Pb and mica Rb-Sr geochronology. Geochemistry, Geophysics, Geosystems 18, 306–332. https://doi.org/10.1002/2016GC006585

Moghadam, H.S., Corfu, F., Chiaradia, M., Stern, R.J., Ghorbani, G., 2014a. Sabzevar Ophiolite, NE Iran: Progress from embryonic oceanic lithosphere into magmatic arc constrained by new isotopic and geochemical data. Lithos 210–211, 224–241. https://doi.org/10.1016/j.lithos.2014.10.004

Moghadam, H.S., Corfu, F., Stern, R.J., 2013a. U–Pb zircon ages of Late Cretaceous Nain Dehshir ophiolites, central Iran. Journal of the Geological Society, London 170, 175–184. https://doi.org/10.1144/jgs2012-066.U

Moghadam, H.S., Mosaddegh, H., Santosh, M., 2013b. Geochemistry and petrogenesis of the Late Cretaceous Haji-Abad ophiolite (Outer Zagros Ophiolite Belt, Iran): Implications for geodynamics of the Bitlis-Zagros suture zone. Geological Journal 48, 579–602. https://doi.org/10.1002/gj.2458

Moghadam, H.S., Stern, R.J., 2015. Ophiolites of Iran: Keys to understanding the tectonic evolution of SW Asia: (II) Mesozoic ophiolites. Journal of Asian Earth Sciences 100, 31–59. https://doi.org/10.1016/j.jseaes.2014.12.016

Moghadam, H.S., Stern, R.J., Chiaradia, M., Rahgoshay, M., 2013c. Geochemistry and tectonic evolution of the Late Cretaceous Gogher–Baft ophiolite, central Iran. Lithos 168–169, 33–47. https://doi.org/10.1016/j.lithos.2013.01.013

Moghadam, H.S., Stern, R.J., Rahgoshay, M., 2010. The Dehshir ophiolite (central Iran): Geochemical constraints on the origin and evolution of the Inner Zagros ophiolite belt. Geological Society of America Bulletin 122, 1516–1547. https://doi.org/10.1130/B30066.1

Moghadam, H.S., Whitechurch, H., Rahgoshay, M., Monsef, I., 2009. Significance of Nain-Baft ophiolitic belt (Iran): Short-lived, transtensional Cretaceous back-arc oceanic basins over the Tethyan subduction zone. Comptes Rendus Geoscience 341, 1016–1028. https://doi.org/10.1016/j.crte.2009.06.011

Moghadam, H.S., Zaki Khedr, M., Chiaradia, M., Stern, R.J., Bakhshizad, F., Arai, S., Ottley, C.J., Tamura, A., 2014b. Supra-subduction zone magmatism of the Neyriz ophiolite, Iran: constraints from geochemistry and Sr-Nd-Pb isotopes. International Geology Review 56, 1395–1412. https://doi.org/10.1080/00206814.2014.942391

Mohammadi, A., Burg, J.-P., Guillong, M., von Quadt, A., 2017. Arc magmatism witnessed by detrital zircon U-Pb geochronology, Hf isotopes and provenance analysis of Late Cretaceous-Miocene sandstones of onshore western Makran (SE Iran). American Journal of Science 317, 941–964. https://doi.org/10.2475/08.2017.03

Moll, M., Paulick, H., Suhr, G., Bach, W., 2007. Data report: microprobe analyses of primary phases (olivine, pyroxene, and spinel) and alteration products (serpentine, iowaite, talc, magnetite, and sulfides) in Holes 1268A, 1272A, and 1274A, in: Proceedings of the Ocean Drilling Program, Scientific Results. Ocean Drilling Program College Station, TX, pp. 1–13.

Monié, P., Agard, P., 2009. Coeval blueschist exhumation along thousands of kilometers: Implications for subduction channel processes. Geochemistry Geophysics Geosystems 10. https://doi.org/10.1029/2009GC002428

Monsef, I., Monsef, R., Mata, J., Zhang, Z., Pirouz, M., Rezaeian, M., Esmaeili, R., Xiao, W., 2018a. Evidence for an early-MORB to fore-arc evolution within the Zagros suture zone: Constraints from zircon U-Pb geochronology and geochemistry of the Neyriz ophiolite (South Iran). Gondwana Research 62, 287–305. https://doi.org/10.1016/j.gr.2018.03.002

Monsef, I., Rahgoshay, M., Pirouz, M., Chiaradia, M., Grégoire, M., Ceuleneer, G., 2018b. The Eastern Makran Ophiolite (SE Iran): evidence for a Late Cretaceous fore-arc oceanic crust. International Geology Review 1–27. https://doi.org/10.1080/00206814.2018.1507764

Morris, A., Meyer, M., Anderson, M.W., MacLeod, C.J., 2016. Clockwise rotation of the entire Oman ophiolite occurred in a suprasubduction zone setting. Geology 44, 1055–1058. https://doi.org/10.1130/G38380.1

Nazemzadeh, M., Rashidi, A., Navazi, M., Poshtkuhi, M., Davari, M., Ezatian, F., Sabzehei, M., Atapour, H., Haddadan, M., 2007. Geological Map of Iran, 1 : 100000 series - Dehsard (Bazar).

Niu, Y., Collerson, K.D., Batiza, R., Wendt, J.I., Regelous, M., 1999. Origin of enriched-type mid-ocean ridge basalt at ridges far from mantle plumes: The East Pacific Rise at 11°20′N. Journal of Geophysical Research: Solid Earth 104, 7067–7087. https://doi.org/10.1029/1998JB900037

Omrani, J., Agard, P., Whitechurch, H., Benoit, M., Prouteau, G., Jolivet, L., 2008. Arc-magmatism and subduction history beneath the Zagros Mountains, Iran: A new report of adakites and geodynamic consequences. Lithos 106, 380–398. https://doi.org/10.1016/j.lithos.2008.09.008

Park, J.-O., Tsuru, T., Kodaira, S., Cummins, P.R., Kaneda, Y., 2002. Splay Fault Branching Along the Nankai Subduction Zone. Science 297, 1157–1160. https://doi.org/10.1126/science.1074111

Patchett, P.J., 1983. Importance of the Lu-Hf isotopic system in studies of planetary chronology and chemical evolution. Geochimica et Cosmochimica Acta 47, 81–91. https://doi.org/10.1016/0016-7037(83)90092-3

Pearce, J.A., 2008. Geochemical fingerprinting of oceanic basalts with applications to ophiolite classification and the search for Archean oceanic crust. Lithos 100, 14–48. https://doi.org/10.1016/j.lithos.2007.06.016

Pearce, J.A., 1996. A users guide to basalt discrimination diagrams. Geological Association of Canada, Short Course Notes.

Pearce, J.A., Lippard, S.J., Roberts, S., 1984. Characteristics and tectonic significance of supra-subduction zone ophiolites. Geological Society, London, Special Publications 16, 77–94. https://doi.org/10.1144/GSL.SP.1984.016.01.06

Pearce, J.A., Stern, R.J., Bloomer, S.H., Fryer, P., 2005. Geochemical mapping of the Mariana arc-basin system: Implications for the nature and distribution of subduction components. Geochemistry, Geophysics, Geosystems 6. https://doi.org/10.1029/2004GC000895

Péron-Pinvidic, G., Manatschal, G., 2009. The final rifting evolution at deep magma-poor passive margins from Iberia-Newfoundland: a new point of view. International Journal of Earth Sciences 98, 1581–1597. https://doi.org/10.1007/s00531-008-0337-9

Pirnia, T., Saccani, E., Torabi, G., Chiari, M., Goričan, Š., Barbero, E., 2019. Cretaceous tectonic evolution of the Neo-Tethys in Central Iran: Evidence from petrology and age of the Nain-Ashin ophiolitic basalts. Geoscience Frontiers S1674987119300647. https://doi.org/10.1016/j.gsf.2019.02.008

Plank, T., 2005. Constraints from Thorium/Lanthanum on Sediment Recycling at Subduction

1294   Zones and the Evolution of the Continents. Journal of Petrology 46, 921–944.
1295   https://doi.org/10.1093/petrology/egi005
1296   Plank, T., Langmuir, C.H., 1998. The chemical composition of subducting sediment and its
1297   consequences for the crust and mantle. Chemical Geology 145, 325–394.
1298   https://doi.org/10.1016/S0009-2541(97)00150-2
1299   Ranero, C.R., von Huene, R., 2000. Subduction erosion along the Middle America convergent
1300   margin. Nature 404, 748–752. https://doi.org/10.1038/35008046
1301   Ricou, L.-E., 1974. L'étude géologique de la région de Neyriz (Zagros iranien) et l'évolution
1302   structurale des Zagrides. (PhD thesis). Université d'Orsay.
1303   Ricou, L.-E., Braud, J., Brunn, J.H., 1977. Le Zagros, in: Livre à La Mémoire de A.F. de
1304   Lapparent (1905–1975), Mémoire Hors-Série de La Société Géologique de France.
1305   Rioux, M., Bowring, S., Kelemen, P., Gordon, S., Dudás, F., Miller, R., 2012. Rapid crustal
1306   accretion and magma assimilation in the Oman-U.A.E. ophiolite: High precision U-Pb zircon
1307   geochronology of the gabbroic crust: OMAN OPHIOLITE ZIRCON GEOCHRONOLOGY.
1308   Journal of Geophysical Research: Solid Earth 117, n/a-n/a.
1309   https://doi.org/10.1029/2012JB009273
1310   Rioux, M., Bowring, S., Kelemen, P., Gordon, S., Miller, R., Dudás, F., 2013. Tectonic
1311   development of the Samail ophiolite: High-precision U-Pb zircon geochronology and Sm-Nd
1312   isotopic constraints on crustal growth and emplacement. Journal of Geophysical Research:
1313   Solid Earth 118, 2085–2101. https://doi.org/10.1002/jgrb.50139
1314   Rioux, M., Garber, J., Bauer, A., Bowring, S., Searle, M., Kelemen, P., Hacker, B., 2016.
1315   Synchronous formation of the metamorphic sole and igneous crust of the Semail ophiolite:
1316   New constraints on the tectonic evolution during ophiolite formation from high-precision U–
1317   Pb zircon geochronology. Earth and Planetary Science Letters 451, 185–195.
1318   https://doi.org/10.1016/j.epsl.2016.06.051
1319   Rollinson, H., 2015. Slab and sediment melting during subduction initiation: granitoid dykes
1320   from the mantle section of the Oman ophiolite. Contributions to Mineralogy and Petrology
1321   170. https://doi.org/10.1007/s00410-015-1177-9
1322   Rossetti, F., Nasrabady, M., Theye, T., Gerdes, A., Monie, P., Lucci, F., Vignaroli, G., 2014.
1323   Adakite differentiation and emplacement in a subduction channel: The late Paleocene
1324   Sabzevar magmatism (NE Iran). Geological Society of America Bulletin 126, 317–343.
1325   https://doi.org/10.1130/B30913.1
1326   Rossetti, F., Nasrabady, M., Vignaroli, G., Theye, T., Gerdes, A., Razavi, M.H., Vaziri, H.M.,
1327   2010. Early Cretaceous migmatitic mafic granulites from the Sabzevar range (NE Iran):
1328   implications for the closure of the Mesozoic peri-Tethyan oceans in central Iran. Terra Nova
1329   22, 26–34. https://doi.org/10.1111/j.1365-3121.2009.00912.x
1330   Sabzehei, M., 1974. Les mélanges ophiolitiques de la région d'Esfandagheh (Iran méridional)
1331   - Etude pétrologique et structurale - Interprétation dans le cadre iranien. Université
1332   Scientifique et Médicale de Grenoble.
1333   Saccani, E., Allahyari, K., Beccaluva, L., Bianchini, G., 2013. Geochemistry and petrology of
1334   the Kermanshah ophiolites (Iran): Implication for the interaction between passive rifting,
1335   oceanic accretion, and OIB-type components in the Southern Neo-Tethys Ocean. Gondwana
1336   Research 24, 392–411. https://doi.org/10.1016/j.gr.2012.10.009
1337   Saccani, E., Delavari, M., Dolati, A., Marroni, M., Pandolfi, L., Chiari, M., Barbero, E., 2018.
1338   New insights into the geodynamics of Neo-Tethys in the Makran area: Evidence from age and
1339   petrology of ophiolites from the Coloured Mélange Complex (SE Iran). Gondwana Research
1340   62, 306–327. https://doi.org/10.1016/j.gr.2017.07.013
1341   Schnur, S.R., Gilbert, L.A., 2012. Detailed volcanostratigraphy of an accreted seamount:
1342   Implications for intraplate seamount formation. Geochemistry, Geophysics, Geosystems 13,
1343   1–13. https://doi.org/10.1029/2012GC004301

1344   Searle, M., Cox, J., 1999. Tectonic setting, origin, and obduction of the Oman ophiolite.
1345   Geological Society of America Bulletin 111, 104–122.
1346   Searle, M.P., 1980. The metamorphic sheet and underlying volcanic rocks beneath the Semail
1347   ophiolite in the Northern Oman mountains of Arabia.
1348   Searle, M.P., Graham, G.M., 1982. "Oman Exotics"—Oceanic carbonate build-ups associated
1349   with the early stages of continental rifting. Geology 10, 43. https://doi.org/10.1130/0091-
1350   7613(1982)10<43:OECBAW>2.0.CO;2
1351   Searle, M.P., Warren, C.J., Waters, D.J., Parrish, R.R., 2004. Structural evolution,
1352   metamorphism and restoration of the Arabian continental margin, Saih Hatat region, Oman
1353   Mountains. Journal of Structural Geology 26, 451–473.
1354   https://doi.org/10.1016/j.jsg.2003.08.005
1355   Seifert, K., Gibson, I., Weis, D., Brunotte, D., 1996. Geochemistry of metamorphosed
1356   cumulate gabbros from Hole 900A, Iberia Abyssal Plain, in: Whitmarsh, R.B., Sawyer, D.S.,
1357   Klaus, A., Masson, D.G. (Eds.), Proceedings of the Ocean Drilling Program, 149 Scientific
1358   Results, Proceedings of the Ocean Drilling Program. Ocean Drilling Program.
1359   https://doi.org/10.2973/odp.proc.sr.149.1996
1360   Shahbazi, H., Siebel, W., Pourmoafee, M., Ghorbani, M., Sepahi, A.A., Shang, C.K.,
1361   Vousoughi Abedini, M., 2010. Geochemistry and U–Pb zircon geochronology of the Alvand
1362   plutonic complex in Sanandaj–Sirjan Zone (Iran): New evidence for Jurassic magmatism.
1363   Journal of Asian Earth Sciences 39, 668–683. https://doi.org/10.1016/j.jseaes.2010.04.014
1364   Shervais, J.W., 1982. TiV plots and the petrogenesis of modern and ophiolitic lavas. Earth
1365   and Planetary Science Letters 59, 101–118. https://doi.org/10.1016/0012-821X(82)90120-0
1366   Sláma, J., Košler, J., Condon, D.J., Crowley, J.L., Gerdes, A., Hanchar, J.M., Horstwood,
1367   M.S.A., Morris, G.A., Nasdala, L., Norberg, N., Schaltegger, U., Schoene, B., Tubrett, M.N.,
1368   Whitehouse, M.J., 2008. Plešovice zircon — A new natural reference material for U–Pb and
1369   Hf isotopic microanalysis. Chemical Geology 249, 1–35.
1370   https://doi.org/10.1016/j.chemgeo.2007.11.005
1371   Söderlund, U., Patchett, P.J., Vervoort, J.D., Isachsen, C.E., 2004. The 176Lu decay constant
1372   determined by Lu–Hf and U–Pb isotope systematics of Precambrian mafic intrusions. Earth
1373   and Planetary Science Letters 219, 311–324. https://doi.org/10.1016/S0012-821X(04)00012-3
1374   Soret, M., Agard, P., Dubacq, B., Plunder, A., Yamato, P., 2017. Petrological evidence for
1375   stepwise accretion of metamorphic soles during subduction infancy (Semail ophiolite, Oman
1376   and UAE). Journal of Metamorphic Geology 35, 1051–1080.
1377   https://doi.org/10.1111/jmg.12267
1378   Spilde, M.N., Brearley, A.J., Papike, J.J., 1993. Alteration of plagioclase and pyroxene
1379   phenocrysts in a fissure fumarole, Valley of Ten Thousand Smokes, Alaska. American
1380   Mineralogist 78, 1066–1081.
1381   Staudigel, H., Koppers, A., Lavelle, J.W., Pitcher, T.J., Shank, T.M., 2010. Box 1: Defining
1382   the word "seamount." Oceanography 23, 20–21.
1383   Stern, R.J., Bloomer, S.H., 1992. Subduction zone infancy: Examples from the Eocene Izu-
1384   Bonin-Mariana and Jurassic California arcs. Geological Society of America Bulletin 104,
1385   1621–1636. https://doi.org/10.1007/s13398-014-0173-7.2
1386   Stern, R.J., Lin, P.-N., Morris, J.D., Jackson, M.C., Fryer, P., Bloomer, S.H., Ito, E., 1990.
1387   Enriched back-arc basin basalts from the northern Mariana Trough: implications for the
1388   magmatic evolution of back-arc basins. Earth and Planetary Science Letters 100, 210–225.
1389   https://doi.org/10.1016/0012-821X(90)90186-2
1390   Stöcklin, J., 1981. A brief report on the geodynamics of Iran. Zagros Hindu Kush Himalaya
1391   Geodynamic Evolution 70–74.
1392   Sun, S.-S., McDonough, W.F., 1989. Chemical and isotopic systematics of oceanic basalts:
1393   implications for mantle composition and processes. Geological Society, London, Special

1394 Publications 42, 313–345. https://doi.org/10.1144/GSL.SP.1989.042.01.19

1395 Tiezzi, L.J., Scott, R.B., 1980. Crystal fractionation in a Cumulate Gabbro, Mid-Atlantic
1396 Ridge, 26°N. Journal of Geophysical Research 85, 5438.
1397 https://doi.org/10.1029/JB085iB10p05438

1398 Tirrul, R., Bell, I.R., Griffis, R.J., Camp, V.E., 1983. The Sistan suture zone of eastern Iran.
1399 Geological Society of America Bulletin 94, 134–150. https://doi.org/10.1130/0016-
1400 7606(1983)94<134

1401 Umino, S., 2012. Emplacement mechanism of off-axis large submarine lava field from the
1402 Oman Ophiolite. Journal of Geophysical Research: Solid Earth 117.
1403 https://doi.org/10.1029/2012JB009198

1404 van der Meer, D.G., van Hinsbergen, D.J.J., Spakman, W., 2018. Atlas of the underworld:
1405 Slab remnants in the mantle, their sinking history, and a new outlook on lower mantle
1406 viscosity. Tectonophysics 723, 309–448. https://doi.org/10.1016/j.tecto.2017.10.004

1407 van Hinsbergen, D.J.J., Maffione, M., Koornneef, L.M.T., Guilmette, C., 2019. Kinematic
1408 and paleomagnetic restoration of the Semail ophiolite (Oman) reveals subduction initiation
1409 along an ancient Neotethyan fracture zone. Earth and Planetary Science Letters 518, 183–196.
1410 https://doi.org/10.1016/j.epsl.2019.04.038

1411 Vervoort, J.D., Blichert-Toft, J., 1999. Evolution of the depleted mantle: Hf isotope evidence
1412 from juvenile rocks through time. Geochimica et Cosmochimica Acta 63, 533–556.
1413 https://doi.org/10.1016/S0016-7037(98)00274-9

1414 Volpe, A.M., Douglas Macdougall, J., Hawkins, J.W., 1988. Lau Basin basalts (LBB): trace
1415 element and SrNd isotopic evidence for heterogeneity in backarc basin mantle. Earth and
1416 Planetary Science Letters 90, 174–186. https://doi.org/10.1016/0012-821X(88)90099-4

1417 Warren, C.J., Parrish, R.R., Waters, D.J., Searle, M.P., 2005. Dating the geologic history of
1418 Oman's Semail ophiolite: insights from U-Pb geochronology. Contributions to Mineralogy
1419 and Petrology 150, 403–422. https://doi.org/10.1007/s00410-005-0028-5

1420 Warren, C.J., Waters, D.J., 2006. Oxidized eclogites and garnet-blueschists from Oman: P-T
1421 path modelling in the NCFMASHO system. Journal of Metamorphic Geology 24, 783–802.
1422 https://doi.org/10.1111/j.1525-1314.2006.00668.x

1423 Whitechurch, H., Omrani, J., Agard, P., Humbert, F., Montigny, R., Jolivet, L., 2013.
1424 Evidence for Paleocene-Eocene evolution of the foot of the Eurasian margin (Kermanshah
1425 ophiolite, SW Iran) from back-arc to arc: Implications for regional geodynamics and
1426 obduction. Lithos 182–183, 11–32. https://doi.org/10.1016/j.lithos.2013.07.017

1427 Wood, D.A., 1980. The Application of a Th-Hf-Ta diagrams to problems of tectonomagmatic
1428 classification and to establish the nature of crustal contaminants of basaltic lavas of the British
1429 Tertiary volcanic province. Earth and Planetary Science Letters 50, 11–30.
1430 http://dx.doi.org/10.1016/0012-821X(80)90116-8

1431 Wrobel-Daveau, J.-C., Ringenbach, J.-C., Tavakoli, S., Ruiz, G.M.H., Masse, P., Frizon de
1432 Lamotte, D., 2010. Evidence for mantle exhumation along the Arabian margin in the Zagros
1433 (Kermanshah area, Iran). Arabian Journal of Geosciences 3, 499–513.
1434 https://doi.org/10.1007/s12517-010-0209-z

1435 Wu, F.-Y., Yang, Y.-H., Xie, L.-W., Yang, J.-H., Xu, P., 2006. Hf isotopic compositions of
1436 the standard zircons and baddeleyites used in U–Pb geochronology. Chemical Geology 234,
1437 105–126. https://doi.org/10.1016/j.chemgeo.2006.05.003

1438 Xu, J.-F., Castillo, P.R., 2004. Geochemical and Nd–Pb isotopic characteristics of the
1439 Tethyan asthenosphere: implications for the origin of the Indian Ocean mantle domain.
1440 Tectonophysics 393, 9–27. https://doi.org/10.1016/j.tecto.2004.07.028

1441 Yamato, P., Agard, P., Goffé, B., de Andrade, V., Vidal, O., Jolivet, L., 2007. New, high-
1442 precision P-T estimates for Oman blueschists: implications for obduction, nappe stacking and
1443 exhumation processes. Journal of Metamorphic Geology 25, 657–682.

1444 https://doi.org/10.1111/j.1525-1314.2007.00722.x
1445 Zamboni, D., Gazel, E., Ryan, J.G., Cannatelli, C., Lucchi, F., Atlas, Z.D., Trela, J., Mazza,
1446 S.E., De Vivo, B., 2016. Contrasting sediment melt and fluid signatures for magma
1447 components in the Aeolian Arc: Implications for numerical modeling of subduction systems.
1448 Geochem. Geophys. Geosyst. 17, 2034–2053. https://doi.org/10.1002/2016GC006301
1449 Zarrinkoub, M.H., Pang, K.N., Chung, S.L., Khatib, M.M., Mohammadi, S.S., Chiu, H.Y.,
1450 Lee, H.Y., 2012. Zircon U-Pb age and geochemical constraints on the origin of the Birjand
1451 ophiolite, Sistan suture zone, eastern Iran. Lithos 154, 392–405.
1452 https://doi.org/10.1016/j.lithos.2012.08.007
1453

1454

1455 Figures:

1456 Fig. 1. Geological context. a) Mesozoic and Cenozoic ophiolites and volcanic arcs along the
1457 Zagros suture zone; b) Detailed zoom of the Hajiabad-Esfandagheh zone, showing the
1458 location of the Siah Kuh unit; c) Paleogeographic map of the Iranian-Omanese Neotethys
1459 during Late Cretaceous. Numbers 1 and 2 indicate two hypotheses for the former location of
1460 the Siah Kuh seamount (see discussion for more details).

1461

1462 Fig. 2. Structural frame: the Siah Kuh seamount (modified after Bonnet et al., 2019). a) Map
1463 of the Siah Kuh unit, the meaning of the color fill for samples is shown on Fig. 2c; b)
1464 Synthetic cross-section of the Siah Kuh seamount; c) Synthetic log of the A and B units, and
1465 proposed correlations (bon. = boninites).

1466

1467 Fig. 3. Field pictures. a) Reef carbonates resting on top of A_1 unit lavas. The granite intrusion
1468 is related to felsic lavas studied hereafter. Rejuvenated magmatism of the $A_{1'}$ unit above the
1469 limestones; b) Sediment intercalation between the A_1 unit and magmatic rejuvenation in the
1470 A unit (A_3); c) Pillow lavas of the core of the seamount; d) Rhyolite dykes in basalt in the core
1471 of the seamount (A_1 unit); e) Anorthosite dyke intruding serpentinite at the base of the B
1472 unit; f) Structure of the northern B unit.

1473

1474 Fig. 4. Microphotographs of representative rocks from the Siah Kuh seamount, from Unit A
1475 (a-c), Unit B (d-f) and felsic associated rocks from both units (g-i). All pictures are at the same
1476 scale and the white horizontal bar represents 500 μm. a) Porphyric texture of sample 1635;
1477 b) Sample 1746 with a phaneritic texture; c) Porphyric texture of sample 1614b; d) Poikilitic
1478 texture of sample 1532, where zircons have been dated; e) Intergranular texture of sample

1479   1735; f) Porphyric texture of sample 1432 where zircons have been dated; g) Porphyric

1480   texture of sample 1601; h) Trachytic texture of sample 1725; i) Phaneritic texture of sample

1481   1720, where zircons have been dated.

1482   Abbreviations are: Cpx: clinopyroxene, Pl: plagioclase, Chl: chlorite, ex-Pl -> Lws:

1483   replacement of magmatic plagioclase by metamorphic lawsonite, Or: orthoclase, Qz: quartz.

1484

1485   Fig. 5. Classification of rocks based on immobile elements. a) Zr/Ti – Nb/Y diagram after

1486   Pearce (1996); b) Th – Co diagram after Hastie et al. (2007). Siah Kuh boninites after

1487   Moghadam et al. (2013b).

1488

1489   Fig. 6. Rare-earth element and multi-element diagrams for all rocks normalized to chondrite

1490   and primitive mantle respectively (Sun and McDonough, 1989). (a, b) Mafic rocks of the core

1491   of the A unit; (c, d) Felsic rocks of the A and B units; (e,f) Magmatic rejuvenation within the A

1492   unit; (g, h) Mafic rocks of B unit, including Siah Kuh boninites (Moghadam et al., 2013b).

1493   Reference spectra are Oman V2 (Alabaster et al., 1982; Godard et al., 2003) and Oman

1494   boninite (Upper V2, Ishikawa et al., 2005; Kusano et al., 2014).

1495

1496   Fig. 7. Trace element discrimination diagrams of mafic rocks. a) Th/Yb vs Nb/Yb diagram by

1497   Pearce (2008), with a density map of the composition of basalts from present-day

1498   seamounts (including intra-oceanic arc seamounts). GLOSS (global subducting sediment)

1499   values from (Plank and Langmuir, 1998) The scale refers to the number of occurrence in the

1500   Georoc database (http://georoc.mpch-mainz.gwdg.de); b) V vs Ti diagram by Shervais

1501   (1982); c) Th-Hf-Ta ternary diagram by Wood (1980); d) Th/La vs Sm/La diagram after Plank

1502   (2005). Siah Kuh boninites after Moghadam et al. (2013b).

1503

1504   Fig. 8. Sr-Nd isotope values for representative rocks of each unit. Cretaceous seawater-rock

1505   mixing line from McCulloch et al. (1981), mixing curve with GLOSS sediment from Plank and

1506   Langmuir (1998). Oman data from Godard et al. (2006), Neyriz from Moghadam et al.

1507   (2014b) and Nain-Baft from Moghadam et al. (2013c).

1508

1509   Fig. 9. Mineral compositions of clinopyroxene and spinel. (a-c) Clinopyroxene discrimination

1510   diagrams in mafic rocks from Leterrier et al. (1982). a) Ti vs Ca + Na diagram showing all

clinopyroxenes plotting in the calk-alkaline to tholeiitic field; b) Ti + Cr vs Ca diagram showing most of the clinopyroxene analyses from the core of the seamount plotting in the orogenic basalts field and other mafic rocks in the non-orogenic tholeiite field; c) Ti vs Al diagram showing that clinopyroxenes from the core of the seamount plot in the arc tholeiite field (other analyses not plotted); d) Cr# vs Mg# diagram for spinel in ultramafic rocks after (Dick and Bullen, 1984) showing all analyses plotting in the supra-subduction zone field.

Fig. 10. Wetherill Concordia diagrams for 4 samples and ^{206}Pb/^{238}U age dispersion plots. a) Rhyolite within A1 (sample 1518), inset shows a zoom on the 70-110 Ma age window; b) Anorthosite within B (sample 1720); c) Gabbro within B (sample 1532); d) Basalt at the top of B (sample 1432), inset shows a zoom on the 70-110 Ma age window. Ages mentioned are weighted averages (*: youngest zircon population).

Fig. 11. Zircon εHf(t) vs age plot showing positive values for most zircons.

Fig. 12. Synthesis of the tectono-magmatic evolution of the Siah Kuh seamount. a) Two stage evolution of the Siah Kuh seamount during late Cretaceous; b) hypothesis 1: Paleogeographic location of the Siah Kuh seamount as a southern intra-Neotethys arc, c) hypothesis 2: paleogeographic location of the Siah Kuh seamount as an intraoceanic arc in the northern Neotethys. Abbreviations are San. for Sanandaj-Sirjan, N.B. for Nain-Baft, C. Iran for Central Iran.

Tables:

Table 1: Sample nature, performed analyses and detailed mineralogy (Gl.= glass).

Table 2: Regional analogs of the Siah Kuh massif in their Neotethyan context: Kermanshah arc (Whitechurch et al., 2013), Kermanshah ophiolitic complex (Ao et al., 2016; Delaloye and Desmons, 1980; Gharib and De Wever, 2010; Ricou et al., 1977; Saccani et al., 2013; Whitechurch et al., 2013; Wrobel-Daveau et al., 2010), Zagros eclogites (Davoudian et al., 2008, 2016), Neyriz ophiolitic complex (Babaie et al., 2006, 2001; Jannessary, 2003; Jannessary and Whitechurch, 2008; Lanphere and Pamić, 1983; Moghadam et al., 2014b; Monsef et al., 2018a; Ricou, 1974), Siah Kuh unit (Moghadam et al., 2013b, this study), South Hajiabad ophiolite (Moghadam et al., 2017, 2013b), Zagros blueschists (Agard et al., 2006;

1543   Angiboust et al., 2016; Moghadam et al., 2017; Monié and Agard, 2009), Sikhoran complex

1544   (Ahmadipour et al., 2003; Ghasemi et al., 2002), Sargaz-Abshur complex (Ghasemi et al.,

1545   2002; Sabzehei, 1974), Oman Exotics (Searle and Graham, 1982), Haybi complex (Searle,

1546   1980), Semail ophiolite (Alabaster et al., 1982; Godard et al., 2003; Guilmette et al., 2018;

1547   Hacker et al., 1996; Ishikawa et al., 2005, 2002; Lachize et al., 1996; Rioux et al., 2016, 2013,

1548   2012; Rollinson, 2015; Soret et al., 2017), Oman blueschists (El Shazly et al., 2001; Searle et

1549   al., 2004; Warren et al., 2005; Warren and Waters, 2006; Yamato et al., 2007), Makran

1550   colored mélange (Burg, 2018; Saccani et al., 2018), Makran blueschists (Delaloye and

1551   Desmons, 1980; Hunziker et al., 2017), Western Iranian Makran (Mohammadi et al., 2017),

1552   Nain-Baft ophiolite (Moghadam et al., 2013a, 2009; Pirnia et al., 2019), Sistan ophiolite

1553   (Babazadeh and de Wever, 2004; Tirrul et al., 1983; Zarrinkoub et al., 2012), Sabzevar

1554   ophiolite (Moghadam et al., 2014a; Rossetti et al., 2014), Sanandaj-Sirjan zone (Arvin et al.,

1555   2007; Jafari et al., 2018; Shahbazi et al., 2010), Urumieh-Dokhtar zone (Omrani et al., 2008)

1556

1557

1558   Supplementary materials

1559   S1: GPS location of samples.

1560   S2: Bulk-rock major and trace element analyses.

1561   S3: Bulk-rock Sr-Nd analyses.

1562   S4: Clinopyroxene EPMA analyses.

1563   S5: Spinel EPMA analyses.

1564   S6: Zircon cathodoluminescence images (concordant)

1565   S7: Zircon U-Pb isotope analyses of concordant zircons.

1566   S8: Zircon trace element data (concordant).

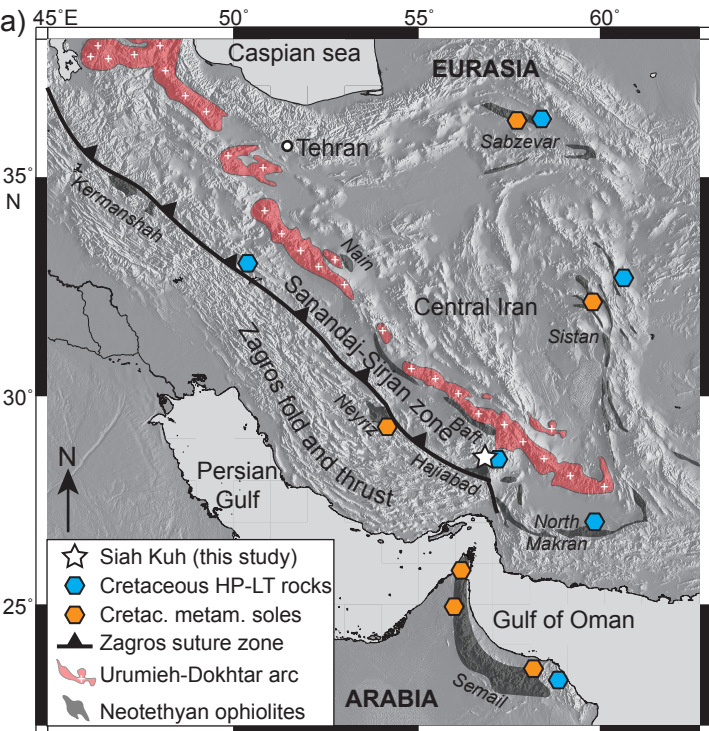1567   S9: Zircon trace element diagram (concordant).

1568   S10: Zircon Lu-Hf isotope analyses of concordant zircons.
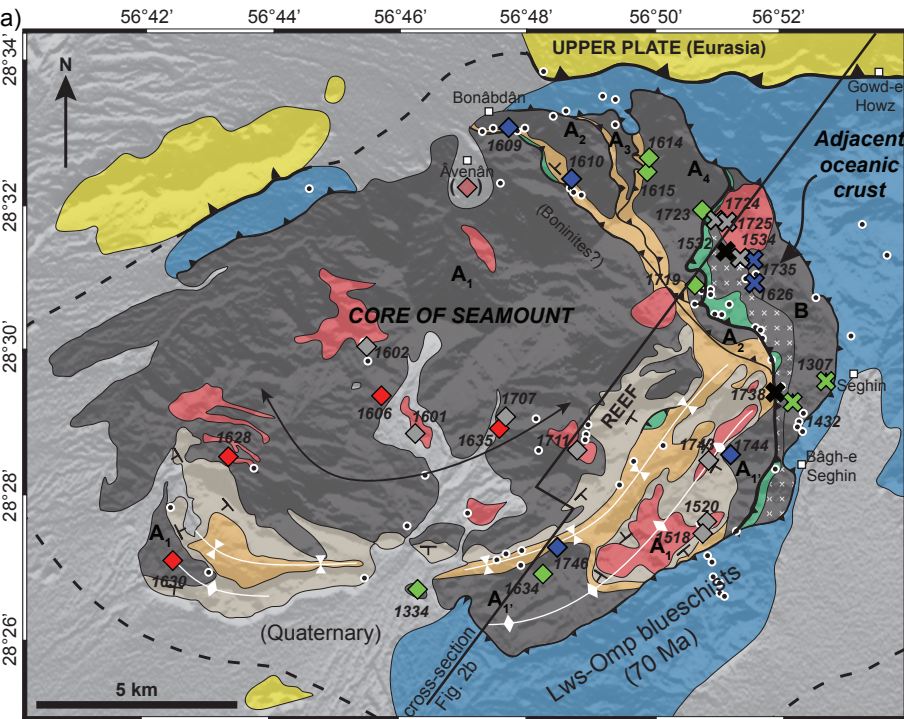
1569   S11: Correlation diagrams between LOI and elements concentrations/isotopic values.

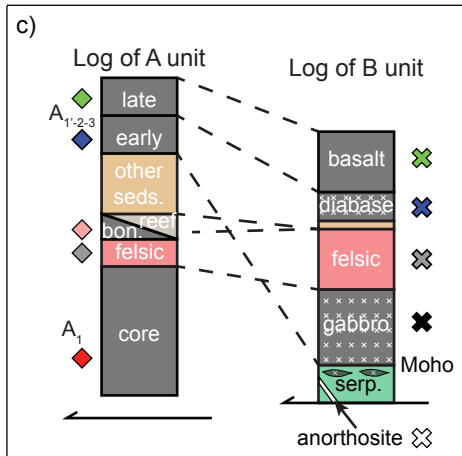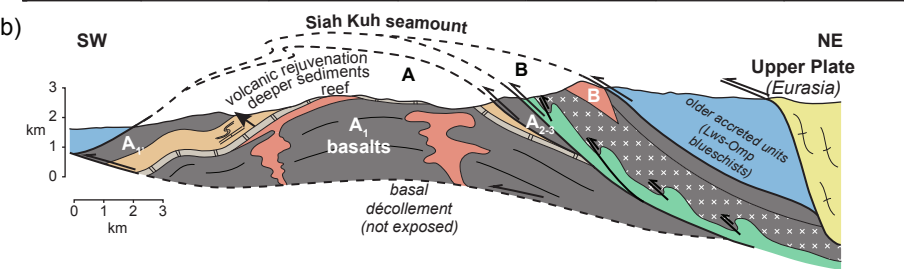1570   S12: Effect of alteration on Sr isotopic signatures.
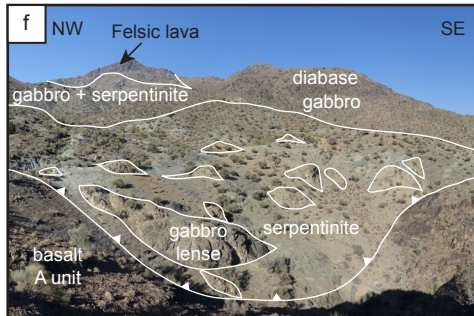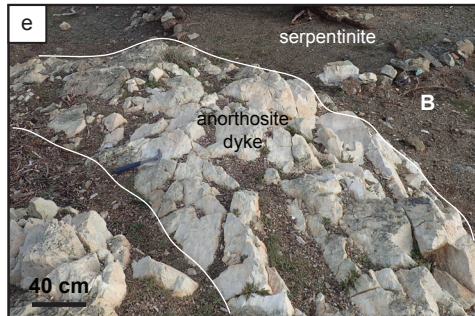
1571

1572

FIG. 1

FIG. 2

FIG. 3

FIG. 4
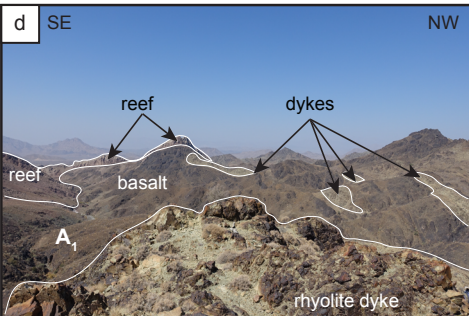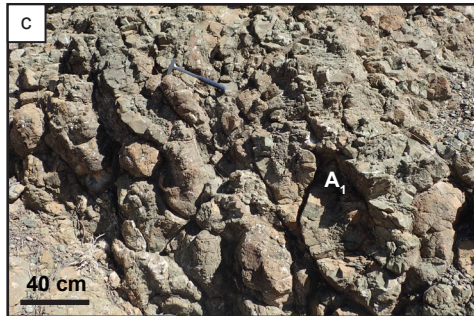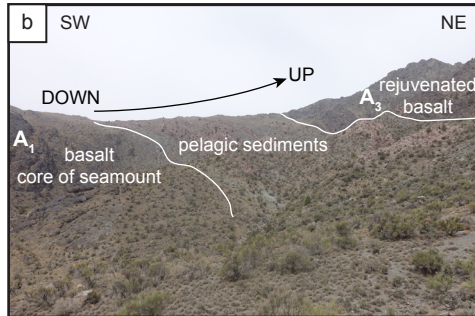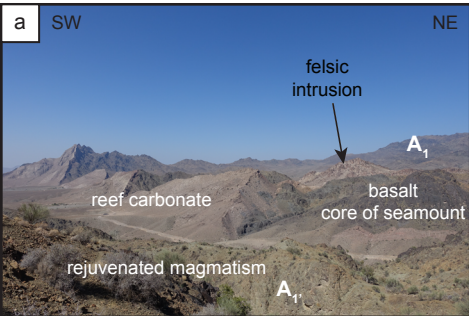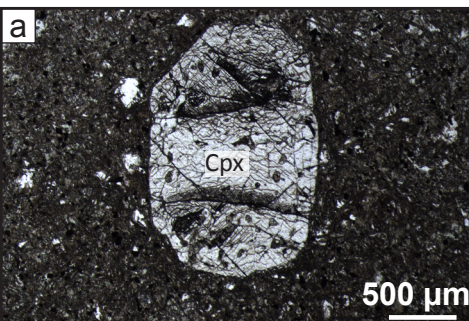
a. Basalt - core of seamount (A$_1$)
b. Basalt - early rejuvenation in A
c. Basalt - late rejuvenation in A
d. Gabbro - base of B unit
e. Diabase - base of B unit
f. Basalt - top of B unit
g. Rhyolite - core of seamount (A$_1$)
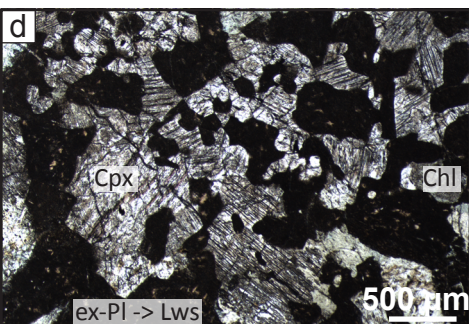h. Rhyolite - B unit
i. Anorthosite - base of B unit
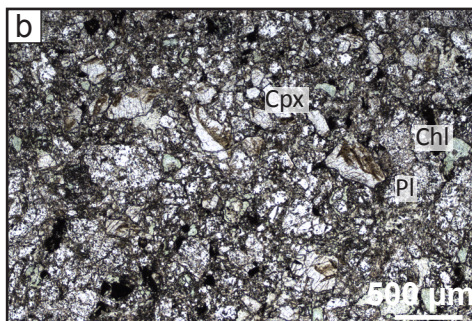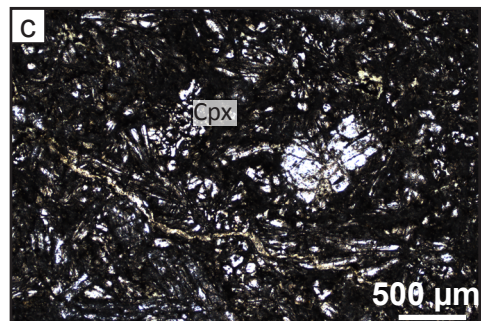
FIG. 5

FIG. 6

g) Mafic rocks in B

h)
- Top of B basalt
- B diabase
- B gabbro

e) Magmatic rejuvenation in A

f)
- Late rejuvenation in A
- Early rejuvenation in A

c) Felsic rocks in A and B

d)
- Felsic rocks in B
- Anorthosite in B
- Felsic rocks in A_1

a) Core of A unit basaltic rocks

1628
Oman V2
Oman boninite   Siah Kuh boninite

b)
Oman V2
Oman boninite
- Siah Kuh boninites
- Seamount core

FIG. 8

Clinopyroxene in basaltic rocks

a)
Ti vs Ca + Na

Legend:
- Top of B basalt
- B diabase
- Base of B gabbro
- Late rejuvenation in A
- Early rejuvenation in A
- Seamount core (A_1)

Alkali basalt

Tholeiitic and calc-alkaline basalt

b)
Ti + Cr vs Ca

Mid-ocean ridge tholeiite

Arc basalt

c)
Ti vs Al

Calc-alkaline basalt

Island arc tholeiite

Spinel in serpentinite

d)
Cr# vs Mg#

SSZ

Abyssal

- B ultramafics (base)
- A ultramafics

FIG. 10

d) Basalt (1432)
B unit

Mean = 73.7 ± 0.7 Ma*
2σ, n = 2/2,
MSWD = 0.31, p(χ²) = 0.58

c) Gabbro (1532B)
B unit

Mean = 77.2 ± 0.4 Ma
2σ, n = 10/13,
MSWD = 0.6, p(χ²) = 0.8

b) Anorthosite (1720)
B unit

Mean = 77.5 ± 0.5 Ma
2σ, n = 9/13
MSWD = 0.5, p(χ²) = 0.8

a) Rhyolite (1518)
A₁ unit

Mean = 87.0 ± 0.9 Ma*
2σ, n = 2/2,
MSWD = 1.4, p(χ²) = 0.23

FIG. 11

FIG. 12

a) **78-73 Ma: Back-arc**

volcanic rejuvenation

A_1-A_4

E- TO N-MORB during subduction after 73 Ma

A_1 basalts

sea level

volcanic rejuvenation

B unit

approx. 5 km

?-87 Ma: Intraoceanic arc

subsidence

REEF

SSZ

A_1 basalts

sea level

B unit

approx. 5 km

b) **Southern Intra-Neotethys Arc - *Hypothesis 1***

S   N

Siah Kuh

③ A_1 87 Ma 'true'arc

A_1-A_4-B 78-73 Ma back-arc extension ④

ARABIA   **EURASIA**

② *Oman* 95 Ma forearc spreading

~150 km

back-arc N.B.

San.   C.Iran

① metam. sole 105-95 Ma

(85 Ma)

mantle upwelling

blueschists 100-65 Ma

c) **Northern Neotethys Arc - *Hypothesis 2***

S   N

Siah Kuh

③ A_1 87 Ma 'true'arc

④ A_1-A_4-B 78-73 Ma back-arc extension

② *Oman* 95 Ma forearc spreading

ARABIA   **EURASIA**

~150 km

back-arc N.B.

San.   C.Iran

① metam. sole 105-95 Ma

(85 Ma)

mantle upwelling

blueschists 100-65 Ma

?

Pelagic sediments
Massive limestone
Felsic volcanics and subvolcanics
Basaltic rocks
Gabbro
Serpentinite

Upper Cretaceous oceanic crust
Early Mesozoic oceanic crust ± OCT
Continental crust

#	Description	Classification	Analyses					Primary						Secondary (alteration)								High P.		
			Trace	Sr-Nd	Cpx	Spl	U-Pb	Cpx	Pl	Or	Qz	Gl.	Ox	Cal	Qz	Chl	Ep	Pmp	Prh	Amp	Srp	Lws	Arg	Amp
1606	Pillow basalt	A1 mafic	x	x	x			x	x			x	x	x	x	x	x							
1628	Basalt	A1 mafic	x					x	x			x	x	x	x					x			x	
1630	Pillow basalt	A1 mafic	x		x			x	x			x	x	x	x		x	x	x					
1635	Basalt	A1 mafic	x	x	x			ex	x			x	x		x	x								
1518	Rhyolite	A1 felsic	x	x			x			x	x	x	x	x			x					x	x	
1520	Rhyolite	A1 felsic	x							x	x	x	x	x			x							
1601	Granitic rock	A1 felsic	x	x					x	x	x		x			x	x	x						
1602	Granitic rock	A1 felsic	x						x	x	x		x			x		x						
1707	Granitic rock	A1 felsic	x						x	x	x		x			x	x							
1711	Rhyolite	A1 felsic	x							x	x	x	x			x		x						
1743	Rhyolite	A1 felsic	x							ex	x	x	x			x								
1609	Basalt	A early rej.	x						x			x	x	x	x	x				x			x	
1610	Basalt	A early rej.	x	x					x			x	x	x	x		x						x	
1744	Basalt	A early rej.	x						x			x	x				x							
1746	Basalt	A early rej.	x	x	x			x	x			x	x			x								
1334	Basalt	A late rej.	x					no thin section																
1614	Basalt	A late rej.	x		x			x	x			x	x		x	x	x							
1615	Pillow basalt	A late rej.	x						x			x	x	x	x		x							
1634	Pillow basalt	A late rej.	x	x				x	x			x	x		x	x	x						x	
1719	Basalt	A late rej.	x						x			x	x	x	x	x								
1723	Basalt	A late rej.	x	x	x			x				x	x			x								
1626	Diabase	B diabase	x	x	x			x	x			x	x			x								
1735	Diabase	B diabase	x		x			x	x				x	x	x							x		
1307	Basalt	B top	x					no thin section																
1432	Basalt	B top	x	x	x		x	x	x			x	x	x	x									
1534	Dacite	B felsic	x	x					x		x	x	x	x	x		x							
1724	Andesite	B felsic	x						x		x		x				x							
1725	Andesite	B felsic	x						x		x		x	x	x									
1532	Gabbro	B gabbro	x		x		x	x	x				x		x		x			x	x	x		x
1738	Gabbro	B gabbro	x					x	x				x	x	x		x			x		x		x
1720	Plagiogranite	B	x				x	x																
1608	Serp. peridotite	A				x							Spl								x			
1533	Serp. peridotite	B				x							Spl								x			
1622	Serp. chromite pod	B				x							Spl								x			
1535	Serp. peridotite	B				x							Spl								x			
1639	Serp. peridotite	B				x							Spl								x			

Locality	Type of rock	Age	Possibly represents?	Reference
Kermanshah arc, Western Zagros	Arc volcanism (Kamyaran)	Paleocene-Eocene	2. North Neotethys arc	Whitechurch et al. (2013)
Kermanshah ophiolitic complex (Harsin-Sahneh), Western Zagros	Bisotun carbonates (shallow sediments) Radiolarite series (deep sediments)	Upper Triassic-Upper Cretaceous Lower Jurassic-"Mid"-Cretaceous	1. rifted allochtons	Ricou (1977); Wrobel-Daveau et al. (2010); Gharib and de Wever (2010)
	Alkaline lavas	Triassic to Liassic	1. rifting	Saccani et al. (2013); Whitechurch et al. (2013)
	IAT	86-81 Ma	3. Cretaceous SSZ magmatism	Whitechurch et al. (2013); Delaloye and Desmons (1980)
	rodingitized gabbro dike in peridotite	79.3	4. Late Cretaceous spreading?	Ao et al. (2016); Wrobel-Daveau et al. (2010)
Zagros eclogites, Western Zagros	Shahrekord eclogite	185-110 Ma	2. North Neotethys subduction?	Davoudian et al. (2008, 2016)
Neyriz ophiolitic complex, Central Zagros	Megalodon limestone (shallow sediments) Pichakun unit (deep sediments)	Upper-Triassic Upper Triassic-"Mid"-Cretaceous	1. rifted allochtons	Jannessary and Whitechurch (2008); Ricou (1974)
	Alkaline lavas	Triassic	1. rifting	Ricou (1974)
	metamorphic sole	94.9 ± 7.6 Ma	3. South Neotethys subduction	Lanphere and Pamić (1983)
	arc tholeiite to boninites	100-92 Ma	3. Cretaceous SSZ magmatism	Moghadam et al. (2014b); Babaie et al. (2006); Jannessary (2003); Lanphere and Pamić (1983); Monsef et al. (2018a)
	calc-alkaline volcanics (Hassanabad unit)	Cretaceous	3. Cretaceous SSZ magmatism	Babaie et al. (2001)
Siah Kuh unit, Eastern Zagros	Arc tholeiites - core of seamount	before 87 Ma? … 95 Ma?	3. Cretaceous SSZ magmatism	Moghadam et al. (2013b); this study
	Felsic volcanism	87 Ma?	3. Cretaceous SSZ magmatism	this study
	MORB magmatism	78-73 Ma	4. Late Cretaceous spreading	this study
South Hajiabad ophiolite, Eastern Zagros	E-MORB lavas	194-186 Ma	1. early spreading	Moghadam et al. (2013b); Moghadam et al. (2017)
Zagros blueschists, Eastern Zagros	Ashin blueschists Seghin blueschists	120-60 Ma	2. North Neotethys subduction	Agard et al. (2006); Monié and Agard (2009); Angiboust et al. (2016); Moghadam et al. (2017)
Sikhoran mafic-ultramafic complex, Eastern Zagros	Gabbroic complexes (contaminated MORB)	250 -180 Ma	1. rifting and early spreding	Ghasemi et al. (2002); Ahmadipour et al. (2003)
	diabasic dykes	160-130 Ma	1. early spreading	Ghasemi et al. (2002)
	E-MORB diabasic dikes	81-76 Ma	4. Late Cretaceous spreading	Ghasemi et al. (2002); Ahmadipour et al. (2003)
Sargaz-Abshur complex, Eastern Zagros	unmetamorphozed sediments	~200 Ma	1. rifting (end)	Sabzehei (1974), Ghasemi et al. (2002)
Oman Exotics, Oman	"Oman exotics" carbonates	Up. Permian to "mid"-Cretaceous	1. rifted allochtons	Searle and Graham (1982)
Haybi complex, Oman	Alkaline lavas	Triassic	1. rifting	Searle (1980)
	E-MORB lavas	Triassic	1. early spreading	Searle (1980)
Semail ophiolite, Oman	metamorphic sole	105 - 95±3 Ma	3. South Neotethys subduction	Hacker et al. (1996); Rioux et al. (2016); Soret et al. (2017); Guilmette et al. (2018)
	V2 volcanism (supra-subduction)	96.4-95.5 Ma	3. Cretaceous SSZ magmatism	Alabaster et al. (1982); Godard et al. (2003); Ishikawa et al. (2002, 2005); Rioux et al. (2012, 2013)
	calc-alkaline felsic intrusives	90-85?	3. Cretaceous SSZ magmatism	Gnos and Peters (1993); Lippard et al. (1986); Searle (1980); Briqueu et al. (1981); Ichikawa et al. (2005); Lachize et al. (1996); Rollinson (2015)
Oman blueschists	As-Sifah blueschists and eclogites	~80 Ma	3. South Neotethys subduction	El Shazly et al. (2001); Searle et al. (2004); Warren et al. (2005); Warren and Waters (2006); Yamato et al. (2007)
Makran colored mélange	Limestone rafts	Permian to Late Jurassic	1. rifted allochtons	Burg (2018)
	Alkaline and arc volcanism	~130 Ma and 95-75 Ma	3. Cretaceous SSZ magmatism?	Saccanni et al. (2018)
Makran blueschists	blueschists	~100 Ma	2. North Neotethys subduction	Delaloye and Desmons (1980); Hunziker et al. (2017)
Western Iranian Makran	detrital zircons in sediments	~105, 95, 85, 76 Ma	2. North Neotethys arc	Mohammadi et al. (2017)
Nain-Baft ophiolite, Northern Zagros	SSZ volcanic rocks	Early Cretaceous-Paleocene	2. North Neotethys back-arc?	Moghadam et al. (2009); Moghadam et al. (2013a); Pirnia et al. (2019);
Sistan ophiolite, E. Iran	MORB to SSZ volcanic rocks	Albian-Paleocene(-Eocene)	2. North Neotethys back-arc	Babazadeh and de Wever (2004); Zarrinkoub et al. (2012); Tirrul et al. (1983)
Sabzevar ophiolite, E. Iran	SSZ volcanic rocks	Aptian-Paleocene(-Eocene)	2. North Neotethys back-arc	Rossetti et al. (2014), Moghadam et al. (2014a)
Sanandaj-Sirjan zone, Northern Zagros	Arc volcanism	Early Jurassic?-Late Cretaceous	2. North Neotethys arc	Arvin et al. (2007); Shahbazi et al. (2010); Jafari et al. (2018)
Urumieh-Dokhtar zone, Northern Zagros	Arc volcanism	Post-Eocene	2. North Neotethys arc	Omrani et al. (2008)

Siah Kuh seamount

volcanic rejuvenation

A_1-A_4

sea level

78-73 Ma

E- TO N-MORB

after 73 Ma
during subduction

volcanic rejuvenation

~87 Ma   SSZ

A_1
basalts

B unit

approx. 5 km

S

N

ARABIA

Oman
95 Ma
forearc
spreading

③ A_1
87 Ma
'true' arc

Siah Kuh A_1-A_4-B
78-73 Ma
back-arc
extension ④

EURASIA

②

~150 km

back-arc
N.B.

San.   C.Iran

(85 Ma)

① metam. sole
105-95 Ma

mantle
upwelling

blueschists
100-65 Ma